

**Flow characteristics downstream of twin pulsed orifice jets: application to  
mitral valve repair**

Maziar Sargordi

A Thesis  
in the Department of  
Mechanical, Industrial and Aerospace Engineering

Presented in Partial Fulfillment  
of the Requirements for the Degree of  
Master of Applied Science (Mechanical Engineering)  
Concordia University  
Montreal, Quebec, Canada

March 2020

© Maziar Sargordi, 2020

**CONCORDIA UNIVERSITY**

**School of Graduate Studies**

This is to certify that the thesis prepared,

By: **Maziar Sargordi**

Entitled: **Flow characteristics downstream of twin pulsed orifice jets: application to mitral valve repair**

and submitted in partial fulfillment of the requirements for the degree of

Master of Applied Sciences (Mechanical Engineering)

complies with the regulations of the University and meets the accepted standards with respect to originality and quality.

Signed by the final Examining Committee:

\_\_\_\_\_  
Dr. Behrooz Yousefzadeh Chair

\_\_\_\_\_  
Dr. Charles Basenga Kiyanda Examiner

\_\_\_\_\_  
Dr. Rolf Wuthrich Examiner

\_\_\_\_\_  
Dr. Lyes Kadem & Dr. Hoi Dick Ng Supervisors

Approved by \_\_\_\_\_  
Dr. S. Narayanswamy, MASc Program Director  
Department of Mechanical and Industrial Engineering

\_\_\_\_\_  
Dr. Amir Asif, Dean,  
Gina Cody School of Engineering and Computer Science

Date \_\_\_\_\_  
March 17, 2020

## **ABSTRACT**

Flow characteristics downstream of twin pulsed orifice jets: application to mitral valve repair

Maziar Sargordi

Mitral regurgitation is the most common valvular insufficiency and Edge-to-Edge Repair (ETER) is a common treatment. This research looks at simplified orifice configurations referred to as Single-Orifice (SO), Symmetric Double-Orifice (SDO) and Asymmetric Double-Orifice (ADO). This research builds on previous experiments performed by Anna Chtchetinina, the data collected are here further post-processed in order to reveal several critical flow characteristics. In the experiments, the unbounded flow is generated through a piston-cylinder setup and time-resolved particle image velocimetry is used for flow measurements. The velocity fields are extracted using a commercial software and then processed using custom-made codes.

Time-averaged velocity profiles of all the configurations show that the two jets merge at the downstream. Also, the investigation on the path of the vortices in the single-orifice configurations displays a steady streamwise velocity of the core through the experiments. The results obtained from analysing energy loss and time-frequency indicate that the symmetric double-orifice presents the most energy dissipation and turbulence among all the configurations. Proper Orthogonal Decomposition (POD) revealed that the asymmetric configuration requires the least number of modes to be reconstructed up to the desired level of energy. POD applied to the strain rate showed that most of the dissipation in single-orifice configuration is present around the center of the vortices.

# Acknowledgements

I would like to express my gratitude to all the people who supported and encouraged me during my master's study.

First, I would like to give my deepest gratitude to my Advisor, Dr. Kadem, for his precious guidance, patience, kindness and support during this time. He was always welcome to my questions and always answered them without hesitation. It was a great pleasure working with you and having your invaluable advice.

I also want to thank Dr. Ng for his guidance and help while conducting this research work. Thanks for giving me the opportunity to work with you.

I wish to express my appreciation for the LCFD lab members whom I collaborated with during this work. I would like to thank Amanda for proofreading this thesis and giving me valuable comments. I also want to thank my other lab mate Ahmed for his endless help. I owe special thanks to Dr. Giuseppe for his unconditional support both in my research and career.

Last but not least, I am forever grateful to my mother, father, sister and my fiancée Beheshteh for being supportive and always believing in me. Indeed, this thesis could not be done without their presence, love and support.

# Table of Contents

List of Figures.....	vii
List of Tables.....	ix
Glossary.....	x
<b>1. Introduction.....</b>	<b>1</b>
1.1. Cardiovascular System.....	1
1.2. Mitral Valve.....	3
1.2.1. Leaflets.....	5
1.2.2. Annulus.....	5
1.2.3. Papillary Muscles and Chordae Tendineae.....	6
1.3. Mitral Valve Regurgitation.....	6
1.4. Mitral Valve Repair.....	8
1.4.1. Annuloplasty.....	8
1.4.2. Quadrangular Resection.....	9
1.4.3. Re-Suspension of Leaflets.....	9
1.4.4. Edge-to-Edge Repair.....	10
<b>2. Literature Review.....</b>	<b>12</b>
2.1.1. Flow Patterns in the Left Ventricle with a Healthy Mitral Valve.....	12
2.1.2. Flow Patterns in the Left Ventricle after ETER.....	12
2.2. Fundamental Studies of Free Jets.....	13
2.2.1. Steady Single Jet.....	13
2.2.1.1. Effect of the Nozzle Type.....	15
2.2.1.2. Effect of the Reynolds Number.....	17
2.2.2. Steady Twin Jets.....	19
2.2.2.1. Twin Plane Jets.....	20
2.2.2.2. Twin Round Jets.....	22
2.3. Pulsatile Jets.....	24
2.4. Objective of the Present Study.....	25
<b>3. Methodology.....</b>	<b>26</b>
3.1. Experimental Apparatus.....	26
3.2. Experimental Procedure.....	27
3.3. Flow Velocity Measurement.....	28

3.4.	Setup Calibration and Validation .....	32
3.5.	Continuous Wavelet Transform .....	34
3.6.	Viscous Energy Dissipation .....	36
3.7.	Proper Orthogonal Decomposition.....	39
<b>4.</b>	<b>Results</b> .....	<b>42</b>
4.1.	Vortex Path in Single Configuration.....	42
4.2.	Flow Visualization .....	43
4.3.	Analysis of Energy Loss .....	47
4.4.	Time-Frequency Analysis .....	50
4.5.	Proper Orthogonal Decomposition.....	53
<b>5.</b>	<b>Conclusions and Recommendations</b> .....	<b>60</b>
	<b>References</b> .....	<b>61</b>
	<b>Appendix</b> .....	<b>66</b>

## List of Figures

<b>Figure 1.1</b> Systematic and pulmonic circulations and capillary networks ( <a href="https://www.vectorstock.com">https://www.vectorstock.com</a> ).....	1
<b>Figure 1.2</b> Systole and diastole phases of one heart cycle ( <a href="https://kids.britannica.com">https://kids.britannica.com</a> ) .....	2
<b>Figure 1.3</b> Schematic of the heart valves in diastole and systole ( <a href="https://www.vectorstock.com">https://www.vectorstock.com</a> ).....	4
<b>Figure 1.4</b> The mitral apparatus ( <a href="http://www.onlinejacc.org/content/65/12/1231/F2">http://www.onlinejacc.org/content/65/12/1231/F2</a> ).....	4
<b>Figure 1.5</b> Saddle-shaped mitral annulus (Jolley et al., 2017).....	5
<b>Figure 1.6</b> Two types of MR: degenerative (primary) and functional (secondary) ( <a href="https://www.bryanhealth.com/medical-providers/the-beat-a-bryan-heart-blog/mitraclip/">https://www.bryanhealth.com/medical-providers/the-beat-a-bryan-heart-blog/mitraclip/</a> ).....	7
<b>Figure 1.7</b> Mitral valve annuloplasty (Murashita et al., 2016) .....	8
<b>Figure 1.8</b> Quadrangular resection for a case with prolapse of the middle scallop of the posterior leaflet ( <a href="https://www.ctsnet.org/article/mitral-valve-repair">https://www.ctsnet.org/article/mitral-valve-repair</a> ).....	9
<b>Figure 1.9</b> Artificial chordae ( <a href="https://www.ctsnet.org">https://www.ctsnet.org</a> ).....	10
<b>Figure 1.10</b> Edge-to-Edge Repair technique ( <a href="https://www.clinicalpainadvisor.com/">https://www.clinicalpainadvisor.com/</a> ).....	10
<b>Figure 1.11</b> Schematic of MitraClip implementation ( <a href="https://www.acc.org">https://www.acc.org</a> ) .....	11
<b>Figure 2.1</b> Schematic of a free turbulent jet.....	14
<b>Figure 2.2</b> Schematic of twin round jets. MP and CP are merging and combined points, respectively ...	19
<b>Figure 3.1</b> Top view schematic of the experimental setup and orifice configurations. The dashed line displays area of investigation captured by the camera .....	27
<b>Figure 3.2</b> Cross-correlation process (Choi et al., 2011) .....	29
<b>Figure 3.3</b> Schematic depicting a typical PIV system ( <a href="http://home.zcu.cz/~rcermak/opvk_htt/VY_01_02.pdf">http://home.zcu.cz/~rcermak/opvk_htt/VY_01_02.pdf</a> ) .....	30
<b>Figure 3.4</b> Schematic of continuous wavelet transform and local matching of the wavelet and the signal (Addison, 2017) .....	36
<b>Figure 3.5</b> Ratio of viscous energy dissipation and kinetic energy. Original signals are displayed on the left. First IMF is subtracted from the signals on the right .....	38
<b>Figure 4.1</b> X-Positions of upper vortices in SO MV are plotted. In the middle figure the noises (frequencies more than 20) are removed using morlet wavelet in wavelet transform. The right figure is a linear estimation. ....	43
<b>Figure 4.2</b> Three formation time of a single-orifice configuration at different instances are presented. $L/D$ from top to bottom is 1.5, 1.9 and 2.5.....	44
<b>Figure 4.3</b> Three MV configurations with $L/D = 1.9$ at different instances are presented. From up to bottom, there are single-orifice MV, symmetric DO MV and asymmetric DO MV.....	45
<b>Figure 4.4</b> Time-averaged velocity profiles of SO MV, symmetric MV and asymmetric MV.....	46

<b>Figure 4.5</b>	Time evolution of VED/KE on the left and time evolution of KE on the right is plotted. ....	48
<b>Figure 4.6</b>	Time evolution of VED/KE on the left and time evolution of KE on the right is plotted .....	49
<b>Figure 4.7</b>	Time frequency spectra of the u-component. The x marks show the points where the signal is obtained.....	51
<b>Figure 4.8</b>	Time frequency spectra of the u-component for symmetric DO with $L/D = 1.9$ for nine points .....	52
<b>Figure 4.9</b>	Time-averaged velocity field and vorticity for all the configurations.....	54
<b>Figure 4.10</b>	Temporal dynamics of the first POD modes .....	55
<b>Figure 4.11</b>	Second spatial POD mode and vorticity for all the configurations .....	56
<b>Figure 4.12</b>	Temporal dynamics of the second POD modes .....	56
<b>Figure 4.13</b>	The fraction of accumulated kinetic energy against mode number.....	57
<b>Figure 4.14</b>	The fractional kinetic energy against mode number. First five modes are plotted separately	58

## List of Tables

<b>Table 3.1</b> Selected seeding particle properties.....	31
<b>Table 3.2</b> Average Reynolds number for different configurations .....	31
<b>Table 3.3</b> Parameters used in the PIV measurement.....	34
<b>Table 4.1</b> Comparison of formation time ratio and core velocity ratio of the upper vortex in SO configuration. The last column is the difference between the $L/D$ ratio and the velocity ratio.....	43
<b>Table 4.2</b> Number of modes required to capture the desired kinetic energy .....	59

## Glossary

$P_c$	Potential core length (m)
$U_j$	Jet centerline velocity (m/s)
$U_{cl}$	Local jet centerline velocity (m/s)
$y_{0.5}$	Half-velocity width (m/s)
Re	Reynolds number
$u_{rms}$	Streamwise velocity (m/s)
$v_{rms}$	Transverse velocity (m/s)
$U_b$	Bulk exit velocity (m/s)
$L$	Length of the ejected fluid (m)
$D$	Nozzle diameter (m)
$x_{MP}$	Streamwise location of the merging point (m)
$x_{CP}$	Streamwise location of the Combined point (m)
$s$	Nozzle spacing (m)
$W$	Nozzle width (m)
$L_f$	Flow characteristic length
$d_p$	Seed diameter (m)
$S_{tk}$	Stokes number
$U_f$	Fluid characteristic velocity (m/s)
$V_x$	Axial velocity (m/s)
$V_y$	Transverse velocity (m/s)
$V_{max}$	Maximum flow velocity (m/s)
$\Delta x_{mm}$	Maximum displacement (m)
$\Delta x_{pix}$	Maximum displacement in pixels (m)
$V_p$	Exit velocity from the nozzle (m/s)
$Q$	Volume flow rate of the piston (m <sup>3</sup> /s)
$A$	Area of the piston (m <sup>2</sup> )
$r$	Radius of the piston (m)

$f_0$	Central frequency of the mother wavelet ( $s^{-1}$ )
$a$	Scale of wavelet
$b$	Location of the wavelet
$T$	Transform function
$R$	Residue
$X$	Velocity matrix
$C$	Correlation matrix
$Q$	Matrix of eigenvectors
$\Lambda$	Diagonal matrix of eigenvalues
$\Phi$	Spatial matrix
$B$	Temporal matrix
$u_{mean}$	Mean velocity magnitude in time (m/s)

### **Acronyms**

MV	Mitral Valve
MR	Mitral Regurgitation
ETER	Edge-to-Edge-Repair
LV	Left Ventricle
LA	Left Atrium
DO	Double Orifice
SO	Single Orifice
SC	Smooth Contraction
MP	Merging Point
CP	Combined Point
PIV	Particle Image Velocimetry
TR-PIV	Time-Resolved Particle Image Velocimetry
POD	Proper Orthogonal Decomposition
CWT	Continuous Wavelet Transform
CCD	Charge - Coupled Device

Nd-YLF	Neodymium-doped Yttrium Lithium Fluoride
CMOS	Complementary Metal-Oxide-Semiconductor
AOI	Area of Interest
IA	Interrogation Areas
S-HGS	Silver-coated Hollow Glass Spheres
PDF	Probability Density Function
WT	Wavelet Transform
STFT	Short-Time Fourier Transform
VEDR	Viscous Energy Dissipation Rate
VED	Viscous Energy Dissipation
EMD	Empirical Mode Decomposition
IMF	Intrinsic Mode Functions
2D	Two Dimensional
<i>KE</i>	Kinetic Energy

### **Greek Symbols**

$\Delta t$	Time interval (s)
$\Delta x$	Displacement (m)
$\rho_p$	Seed density ( $\text{kg}/\text{m}^3$ )
$\tau_p$	Particle relaxation time (s)
$\tau_f$	Characteristic time scale of the fluid
$\mu$	Viscosity ( $\text{kg}/\text{ms}$ )
$\alpha$	Calibrated scale factor
$\Psi$	Wavelet
$\Gamma_2$	Gamma-two vortex criteria

# 1. Introduction

## 1.1. Cardiovascular System

The cardiovascular system permits blood to circulate and transports nutrients, electrolytes, oxygen, carbon dioxide, hormones, and blood cells to and from the cells in the body, see Fig. 1.1. Furthermore, the cardiovascular system, also called the circulatory system, helps in fighting diseases, and stabilizes temperature and pH.

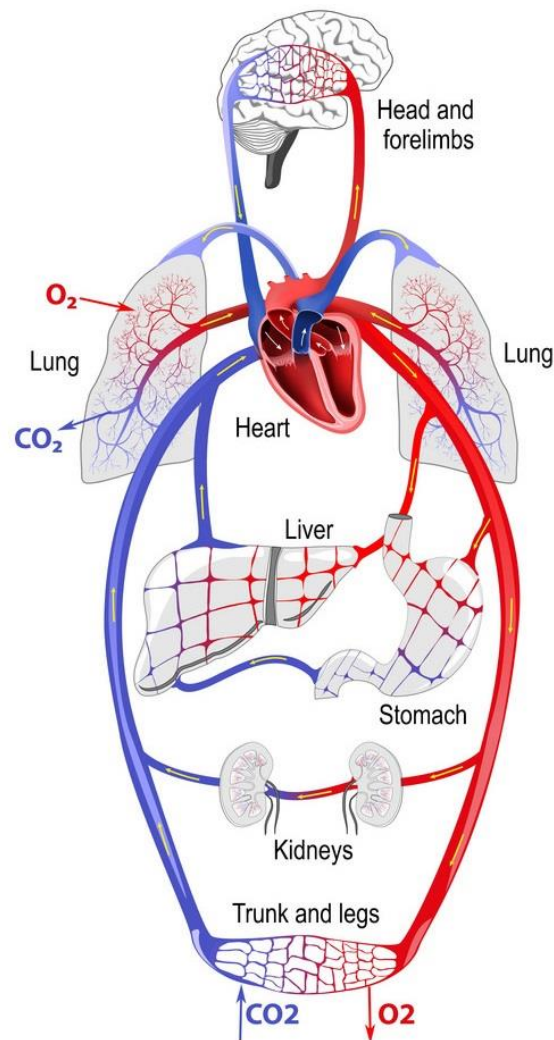


**Figure 1.1** Systematic and pulmonic circulations and capillary networks  
(<https://www.vectorstock.com>)

The heart, the blood and the blood vessels are the main components of the human cardiovascular system. The other types of circulatory systems are the pulmonary circulation, which is a closed path through the lungs where blood is oxygenated, and the systemic circulation, which is a closed path through the rest of the body that provides oxygenated blood (Fig. 1.1). In addition, the digestive system provides the required nutrients to the body and helps to keep the heart pumping functionality (Guyton & Hall, 2015). The cardiovascular system is a closed path, and the blood never leaves the network of blood vessels. In contrast, oxygen and nutrients diffuse across the blood vessel layers. They enter the interstitial fluid to carry oxygen and nutrients to the cells and take carbon dioxide and wastes from the cells. When the heart beats, the blood circulates through the pulmonary and systemic circuits of the body, shown in Fig. 1.2.

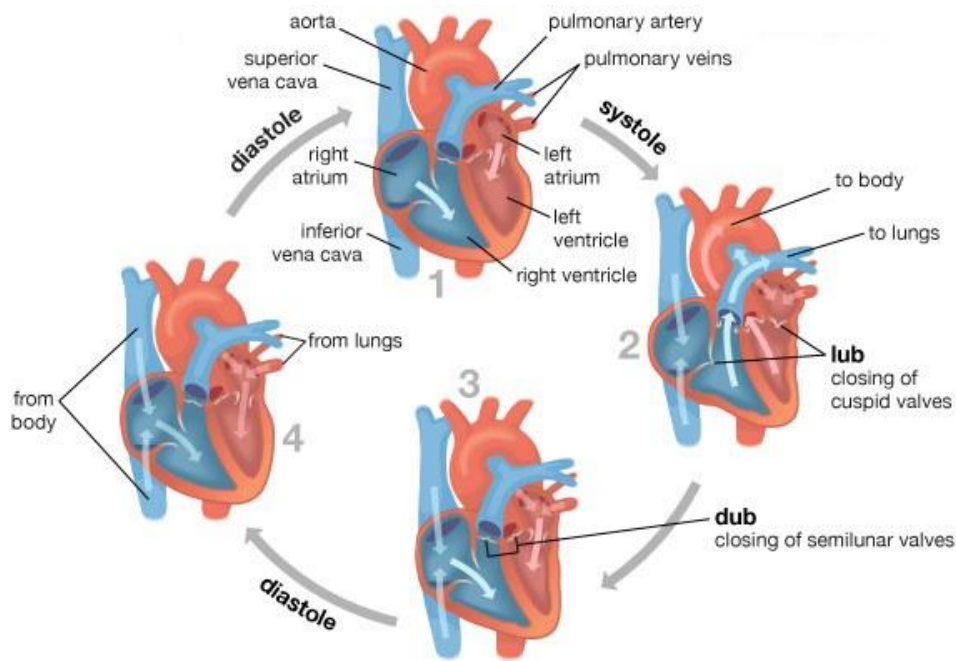


**Figure 1.2** Systole and diastole phases of one heart cycle (<https://kids.britannica.com>)

Diastole and systole are the two main phases in the cardiac cycle. In diastole, the ventricles are relaxed, and the heart is filled with blood. During systole, the ventricles contract and the blood is pumped out of the heart and towards the arteries. When the heart chambers fill with blood which is then pumped out of the heart, one cardiac cycle is completed.

## **1.2. Mitral Valve**

Heart valves act as check valves to prevent blood from back flowing. They remain closed until the upstream pressure is enough to force the blood to move forward. Four cardiac valves which do the task of guiding the blood flow through diastole and systole can be found in Fig 1.3.

The mitral valve (MV) prevents blood from flowing backward into the pulmonary veins and therefore into the lungs. Even when the pressure in the left ventricle (LV) is very high, the mitral valve prevents the backward flowing (Waite & Fine, 2007). The diastolic blood flow is guided from the left atrium (LA) to the left ventricle through the mitral valve. Also, it prevents blood backflow from the left ventricle into the left atrium.

The mitral valve consists of the annulus, the leaflets, the papillary muscles, and the chordae tendineae (Mauro et al., 2013). They all have a role in the optimal functioning of the mitral valve. Moreover, the contraction and the relaxation of the left atrium have important role in the functionality of the mitral valve. It is confirmed that the closure of the mitral valve is a result of atrial contraction and relaxation (Perloff & Roberts, 1972).

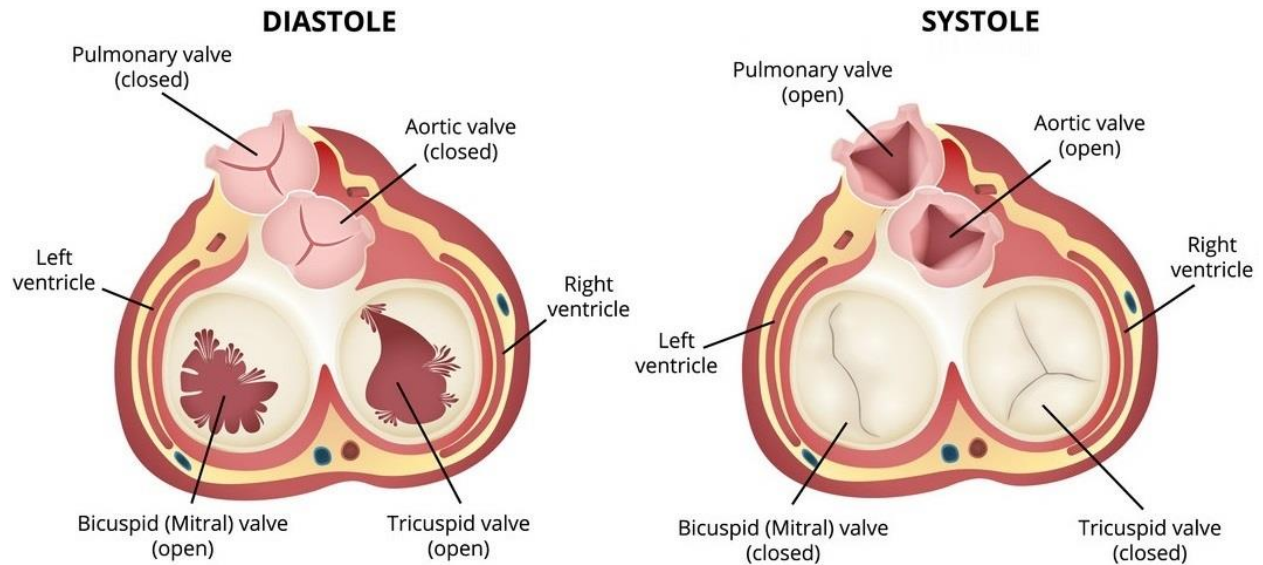


**Figure 1.3** Schematic of the heart valves in diastole and systole (<https://www.vectorstock.com>)

It is also worth mentioning that although the onset of LV systole is not required for coaptation of the mitral leaflets at the end of atrial systole, it is actually the LV systole that results in the complete closure of the leaflets by causing the motion of the mitral leaflets towards the mitral annular plane (Kaul, 2004).

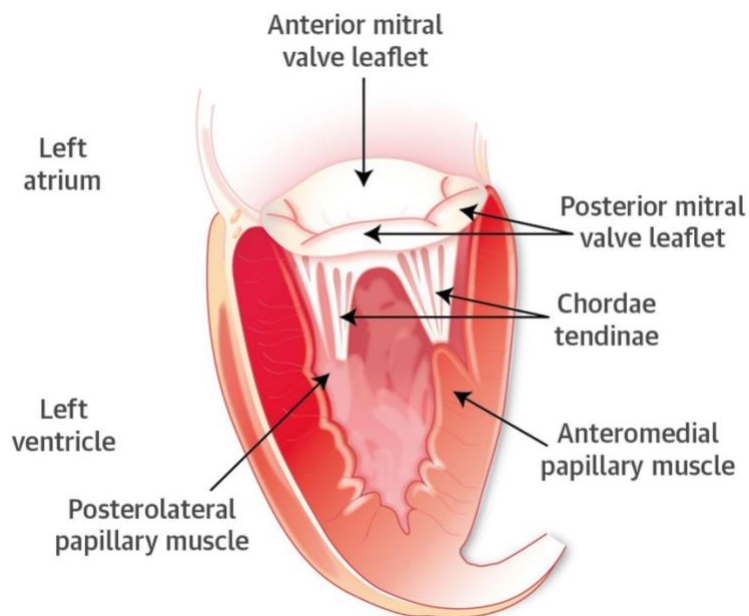


**Figure 1.4** The mitral apparatus (<http://www.onlinejacc.org/content/65/12/1231/F2>)

### 1.2.1. Leaflets

Based on the orientation of the leaflets, they can either be called antero-superior or infero-posterior (Di Mauro et al., 2013). However, they are more commonly known as the anterior and posterior leaflets (McCarthy & Ring & Rana, 2010). The two leaflets of the mitral valve have different structures. In fact, two-thirds of the circumference of the left atrioventricular junction are occupied by the posterior leaflet and are relatively narrow, while the anterior leaflet is broader and comprises the rest of the annular circumference. In adults, there are three scallops along the posterior free edge (McCarthy et al., 2010).

### 1.2.2. Annulus

The mitral valve has a three-dimensional structure, as shown in Fig. 1.5. However, in a two-dimensional view it is more of a D-shaped annulus rather than a circular one. The annulus also has a longer inter-commissural diameter than the septo-lateral one (Di Mauro et al., 2013).

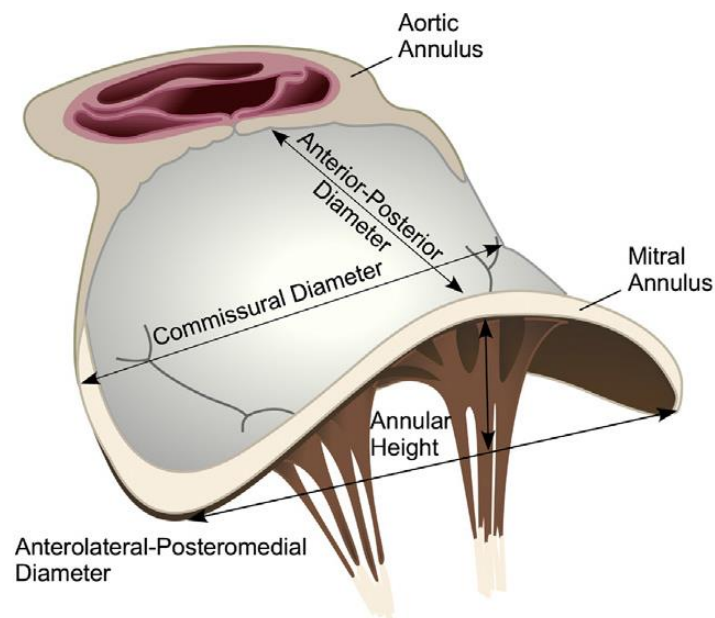


**Figure 1.5** Saddle-shaped mitral annulus (Jolley et al., 2017)

It can be observed in annulus anatomy that there is a saddle-shaped configuration where the highest point is along the anterior annulus and the lowest point is at the level of the commissures (Di Mauro et al., 2013).

### **1.2.3. Papillary Muscles and Chordae Tendineae**

The papillary muscles act as shock absorbers to compensate for the geometric changes in the left ventricular wall (Di Mauro et al., 2013). The papillary muscles are in the anterolateral and posteromedial positions, as shown in Fig. 1.4. They are usually attached at the border of the anterolateral and infero-lateral walls. In addition, some of them are also positioned over the inferior wall of the left ventricle along the mid to apical segments. In most adults, the papillary muscles may have up to three heads (McCarthy et al., 2010). To form the tensor apparatus of the valve, the tendinous cords of the mitral valve relate the leaflets to two groups of papillary muscles and to the posterior muscular wall (Di Mauro et al., 2013).

## **1.3. Mitral Valve Regurgitation**

Mitral regurgitation (MR) is the leakage of blood backward into the left atrium when the left ventricle contracts, (see Fig. 1.6). MR can be classified into two groups: primary and secondary MR. Primary MR is due to biological changes in the mitral valve tissue leading to the weakening of the leaflets and chordae and resulting in their rupture. This leads to incomplete closure of the leaflets during systole (see Fig. 1.6). In secondary MR, regurgitation happens due to the reduction and/or elimination of the normal systolic coaptation of the leaflets of the mitral valve (Ducas et

al., 2014). In both cases, blood flows backward into the left atrium during systole. Therefore, it alters ventricular preload and afterload.

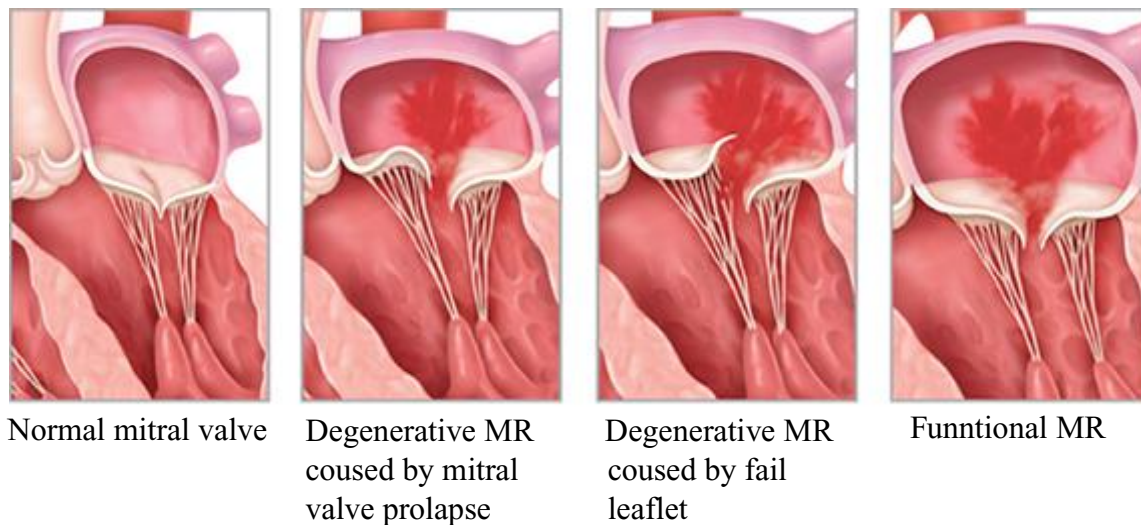


**Figure 1.6** Two types of MR: degenerative (primary) and functional (secondary) (<https://www.bryanhealth.com/medical-providers/the-beat-a-bryan-heart-blog/mitraclip/>)

The addition of regurgitant blood volume to the pulmonary venous inflow raises diastolic ventricular pressure and wall stress. Also, it results in structural and functional deterioration of the left ventricle. Initially systolic afterload is reduced with MR. However, the increase in ventricular radius and the reduction in ventricular wall thickness cause elevation of the afterload over time. This irreversible transition results in congestive heart failure over time.

When regurgitation happens, the heart needs to work harder in order to keep pumping the blood at the same rate. This extra work weakens the heart and leads to congestive heart failure. This regurgitation also may cause pulmonary edema due to the backwards flow into the pulmonary system. Another frequent problem caused by regurgitation is atrial fibrillation. Furthermore, regurgitation can also increase left atrium pressure which leads to pulmonary hypertension and heart failure on the right side of the heart (Espiritu et al., 2013; Vahanian et al., 2012; Grigioni et

al., 2002; Barbieri et al., 2010). Ninety percent of the patients with primary MR survive after 8 years past the diagnosis of MR and 50% survive for their whole life. In contrast, only 30% of patients with secondary MR live without any cardiac events after 5 years. Around 10% of the people over of the age 75 are suffering from MR and it is the second most common disease that requires surgery in Europe (Espiritu et al., 2017).

## 1.4. Mitral Valve Repair

Surgical mitral valve intervention is currently considered as the best option for treatment of symptomatic patients with severe degenerative MR (Bonow et al., 1998). Several reports have indicated the superiority of MV repairs over MV replacements based on having better preservation of LV function, lower thrombus formation, and more survival rates (Gillinov et al., 2008).

Current MV repair techniques are: annuloplasty, quadrangular resection, resuspension of leaflets, and Edge-to-Edge Repair (ETER).

### 1.4.1. Annuloplasty

In annuloplasty, a surrounding device is placed around the mitral valve in order to restore its physiological form. Therefore, annuloplasty ensures the optimal coaptation of the valve leaflets and minimizes regurgitation, as shown in Fig. 1.7.

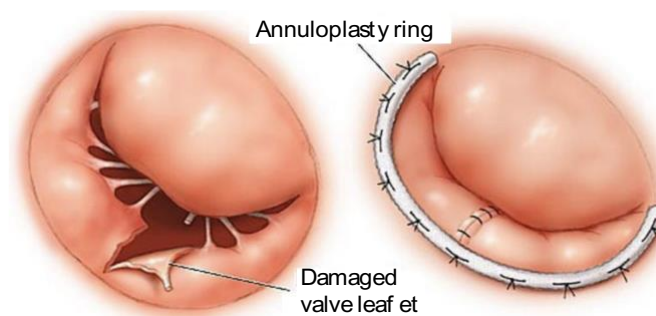


**Figure 1.7** Mitral valve annuloplasty (Murashita et al., 2016)

### 1.4.2. Quadrangular Resection

Prolapse of the middle portion of the posterior leaflet may result from the rupture of the chordae tendineae. Quadrangular resection is implemented in combination with either mitral annulus, sliding annuloplasty or folding plasty (Holubec et al., 2013). The goal in quadrangular resection is to restore the original shape of the MV by removing the loose segments of the leaflets (see Fig. 1.8). However, the anatomy of the MV and the physiological role of the posterior leaflet are not retained in quadrangular resection (Holubec et al., 2013).

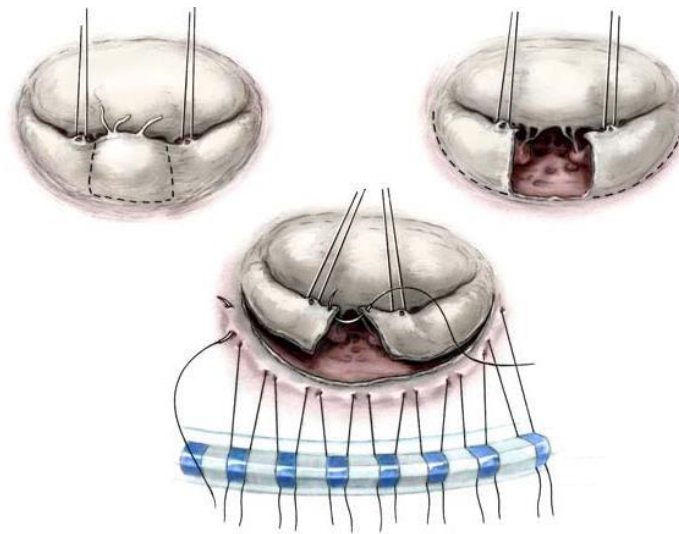


**Figure 1.8** Quadrangular resection for a case with prolapse of the middle scallop of the posterior leaflet (<https://www.ctsnet.org/article/mitral-valve-repair>)

### 1.4.3. Re-Suspension of Leaflets

To support MV with elongated or broken chords, artificial chordae tendineae are used to prevent prolapsing. Additional chords also might be used to hold loosen leaflets, see Fig. 1.9.

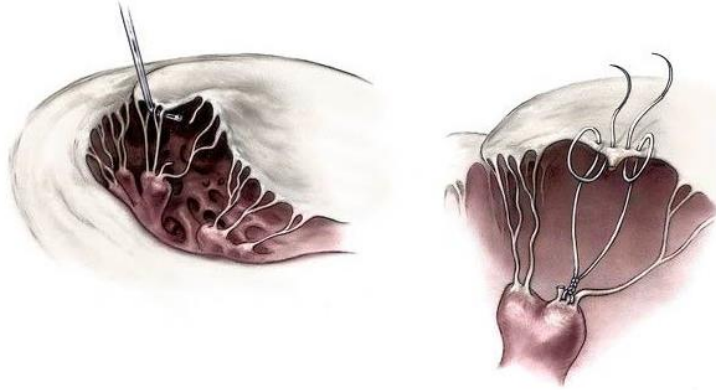


**Figure 1.9** Artificial chordae (<https://www.ctsnet.org/>)

#### 1.4.4. Edge-to-Edge Repair

Edge-to-Edge Repair (ETER) was first developed by Alfieri et al. (2001). The surgical technique is simple and consists of suturing the free edges of the mitral valve leaflets at the location where there is regurgitation present, as given in Fig. 1.10.



**Figure 1.10** Edge-to-Edge Repair technique (<https://www.clinicalpainadvisor.com/>)

The proper implementation of ETER leads to low risk and good early to mid-term clinical results (Maisano et al., 2000). ETER significantly modifies the flow patterns in the left ventricle (LV) and leads to a double-orifice (DO) in the MV opening. Under such valve opening configuration, the induced flow in the LV is mostly unknown. Despite the previous mentioned methods, almost half

of the patients with symptomatic severe MR are considered at high risk and are not eligible to undergo an open-heart surgery (Goel et al., 2014). This procedure also can be minimally invasive by using a MitraClip (Rogers & Franzen, 2011), see Fig. 1.11. However, the traditional surgical method is the preferred treatment for the majority of patients (<https://www.ottawaheart.ca/test-procedure/mitraclip>).

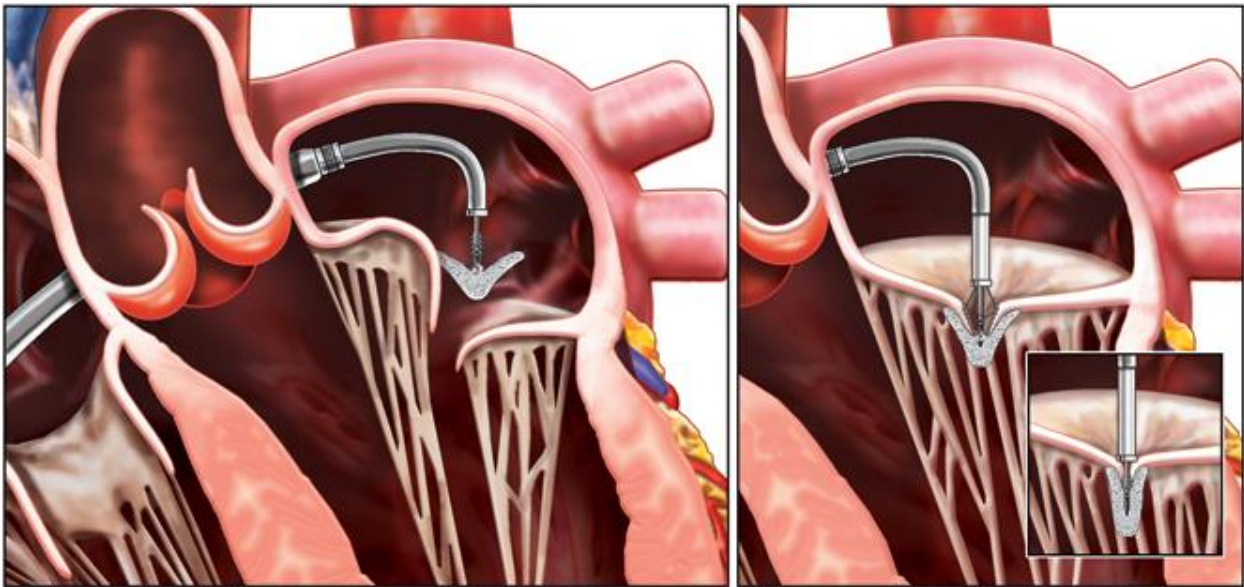


**Figure 1.11** Schematic of MitraClip implementation (<https://www.acc.org>)

In the next chapter, we review the previous related studies done in the context of steady and pulsatile jets through single orifices and multiple/twin orifices.

## **2. Literature Review**

ETER leads to an interesting flow structures in the LV that are characterized by twin jets. This has not been thoroughly investigated in the literature. However, extensive work has been done regarding steady jets through single orifice and multiple/twin orifices. In this literature review, the work dedicated to single orifices and twin orifices are described in detail.

### **2.1.1 Flow Patterns in the Left Ventricle with a Healthy Mitral Valve**

In a healthy heart, a vortex ring is created during the E-wave. This vortex ring stores the kinetic energy of the blood and it minimizes the energy dissipation (Sotiropoulos et al., 2016; Faludi et al., 2010). Many cardiac function aspects are reflected uniquely by the optimization of vortex formation in the blood flow during early diastole (Gharib et al., 2006). When a fluid's boundary layer is separated due to a sharp edge, vortices are created. Laminar inflow is transformed into a vortex ring in the left ventricle at the tips of the mitral valve leaflets. This minimizes the energy loss during LV filling (Faludi et al., 2010). Energy loss in a vortex is a consequence of rapid changes in the vorticity of a viscous flow. Also, interactions between many small vortices lead to energy losses. Therefore, a single large vortex is favorable to preserve the energy of the flow. An increase in the energy loss requires the heart to work harder (Faludi et al., 2010). Apart from energy preservation, efficient vortex formation helps the normal leaflet coaptation at mid-diastole (Ghosh & Kovacs, 2011).

### **2.1.2. Flow Patterns in the Left Ventricle after ETER**

Percutaneous mitral edge-to-edge repair significantly modifies the flow patterns in the left ventricle and leads to a double-orifice in the MV opening. Under such valve opening configuration, the evaluation of MV hemodynamics is mostly unknown regarding induced flow patterns in the

LV. Numerical simulations by Maisano et al. revealed that the downstream velocity profile of double-orifice MV is almost the same as in a healthy single-orifice (SO) (Maisano et al., 1999). They also demonstrated that there is a 35 percent pressure difference between SO and DO in the centerline. Another numerical study by Hu et al. (2010) revealed that there are major energy losses in a DO MV. They also showed that MV edge-to-edge repair lowers LV filling efficiency. However, keeping the orifices large may help to prevent the increase in energy loss.

## **2.2. Fundamental Studies of Free Jets**

### **2.2.1. Steady Single Jet**

A turbulent jet is generated once a high momentum fluid is discharged into the ambient fluid. A free jet, which is the subject of this thesis, is created when the discharged jet is sufficiently far away from a free surface or solid boundary that its development is not affected by the boundary. Turbulent jets may be created from a long pipe, smooth contraction or an orifice nozzle (Mi et al., 2001; Mi et al., 2001). They might issue from symmetric (round) or asymmetric nozzles (e.g. ellipse or rectangle). Depending on the application, turbulent jets may be created from single or multiple nozzles. Figure 2.1 shows a schematic of a round jet generated from a smooth contraction nozzle. The subsequent three distinct regions of the flow are identified as: near field, intermediate field and far field (self-similar region). The potential core, where the flow characteristics match those of the nozzle exit, is located within near field. The potential core length ( $P_c$ ) is typically defined as the distance from the jet exit plane to the point where the centerline velocity decays to  $0.98U_j$ , where  $U_j$  is a velocity on the jet centerline. However,  $0.98U_j$  is not universal, and in some studies, it was chosen to be  $0.95U_j$  (Bogey & Bailly, 2006) or  $0.9U_j$  (Murakami & Papamoschou,

2002). The intermediate region is found between the near and far field regions. In the self-similar region, the mean and turbulent statistics could be represented by normalized parameters that only rely on one velocity scale and one length scale (George, 1989; Pope, 2000). The velocity and length scales that are widely used are the local jet centerline velocity ( $U_{cl}$ ) and half-velocity width ( $y_{0.5}$ ). The half-velocity width represents the distance from the jet centerline to the point where the streamwise mean velocity is half the centerline velocity. In the self-similar region, the velocity decay and jet spread increase almost linearly with streamwise distance from the jet exit plane. It ought to be noted that these three regions also are applicable to noncircular single jets as well as jets generated from long pipes and orifice nozzles.

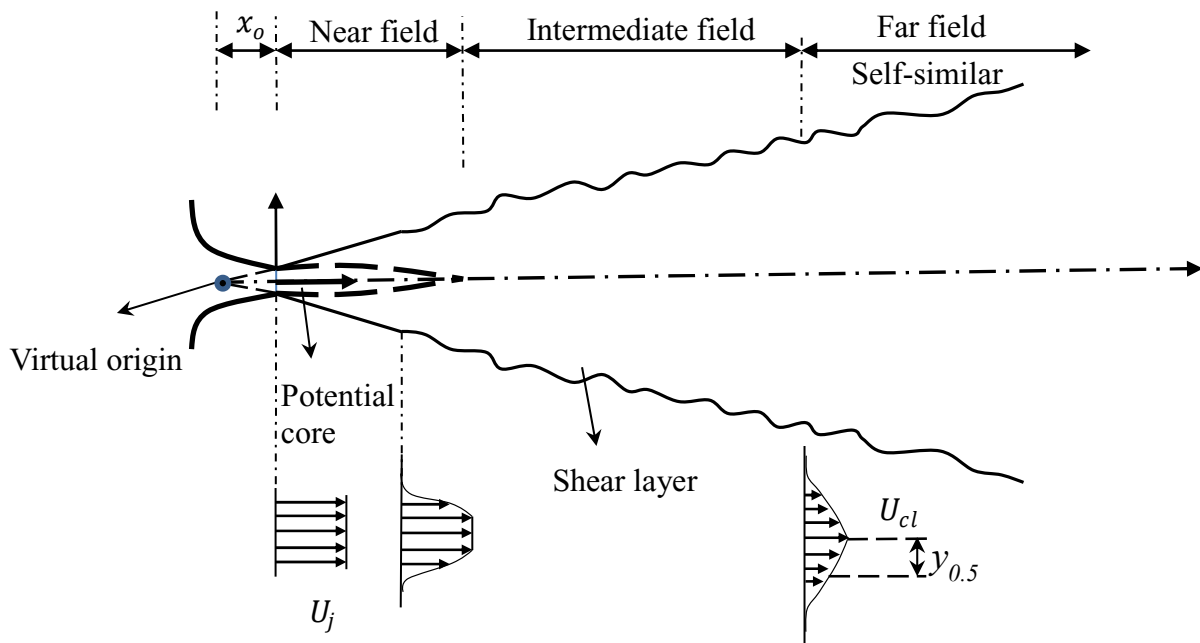


**Figure 2.1** Schematic of a free turbulent jet

Because of large velocity gradients within the radial direction and due to Kelvin-Helmholtz instability, vortex rings form, evolve and pair-up to create large eddies in the shear layer (Hu et al., 2000). Those large eddies wreck down into smaller eddies, and for this reason, the turbulent

structures decrease in scale. In this process, energy is transferred from the larger scale structures to the smaller scale ones. Additionally, vortex formation and pairing process are fundamentally important in the mixing of the jets with the ambient flow (Abdel-Rahman et al. 2010).

Single jets are studied extensively in the literature. Plane and round jets are the simplest forms due to their statistical properties such as turbulence intensities and the mean velocities can be represented by two independent spatial variables in the near and intermediate regions. Turbulence intensity is defined as the ratio of the root-mean-square of the velocity fluctuations to the mean flow velocity. A faster increase in turbulence intensity from the inlet value to its maximum value is an indication of more mixing in the near region of a jet.

In the far region where the flow becomes self-similar, just one spatial variable is enough to describe the statistical properties (George, 1989; Pope, 2000). Therefore, most of the previous studies focused on round and plane jets due to their geometric simplicity (Wynanski & Fiedler, 1969; Hussain & Clark, 1977; Quinn & Militzer, 1989; Panchapakesan & Lumley, 1993; Richards & Pitts, 1993; Boersma et al., 1998; Ferdman et al., 2000; Antonia & Zhao, 2001). Richards & Pitt (1993) and Antonia & Zhao (2001) concluded that the self-similar state is a universal state and it is independent of the initial conditions. However, some studies suggest that it is unlikely to have a universal self-similar state (Wynanski & Fiedler, 1969; George, 1989; Mi et al., 2001).

### **2.2.1.1. Effect of the Nozzle Type**

As discussed previously, there are three nozzle types: orifice, smooth contraction (SC) and pipe. The effects of nozzle type on the evolution of jet flows are investigated extensively (Mi et al., 2001; Mi et al., 2001; Xu & Antonia, 2002; Quinn, 2006). The study done by Mi et al. (2001) on

round jets showed that the inlet streamwise mean velocity is strongly dependent on the type of nozzle. For example, the mean velocity profiles at the exit of smooth contraction, orifice nozzle and pipe respectively follow flat-like, saddle-backed and one-seventh power law distributions. Occurrence of the vena contracta effect is an important characteristic of orifice jets. First, there is a sudden contraction in the fluid stream, and then shortly after the nozzle plate, the jet cross section reaches to its minimum and the velocity reaches its maximum.

Quinn (2006) compared the flow properties of jets resulting from smooth contraction and orifice nozzles at  $Re = 184000$ . The results revealed that in the orifice jet the potential core length was 20% shorter and the centerline turbulence intensity reached its highest point faster. Furthermore, the normalized streamwise,  $u_{rms}/U_e$  and transverse  $v_{rms}/U_e$ , turbulence intensities reached their highest point at  $x/D = 8$  in the orifice jet but the location for the maximum intensities is delayed to  $x/D = 9$  in the smooth contraction jet. In the self-similar region, the velocity decay and spread rates were 2% higher in the orifice jet in comparison to the smooth contraction jet. Therefore, the results indicated that the orifice jet had a higher mixing performance compared to the smooth contraction jet.

Quinn (2006) and Mi et al. (2001) analyzed one dimensional energy spectra of velocity fluctuations in turbulent jets generated from pipe, smooth contraction and orifice nozzles. A broad peak was observed for the orifice and smooth contraction jets, while no peak was present in the spectra for the pipe jets. They concluded that the broad peaks are indicative of a quasi-periodic passage of coherent structures in the smooth contraction and orifice jets, and non-periodic structures in the pipe jets. The higher magnitudes of the peaks in spectral analyses also indicated the presence of more energetic structures in the orifice jet.

### 2.2.1.2. Effect of the Reynolds Number

The Reynolds number (Re), defined based on the nozzle diameter (or slot width for plane jets) and jet inlet velocity (Hussain & Clark, 1977; Namer & Otügen, 1988; Deo et al., 2007; Quinn et al., 2013; Xu et al. 2014) is another influential parameter impacting on the characteristics of turbulent jets. Namer & Ötügen (1988) investigated the effects of Reynolds number on plane jets over the range of Re from 1000 to 7000. It was observed that the turbulence intensity in the near region grew at increasing rates with the increase of Re, while the potential core length became smaller. The results showed that the distance from the exit of the nozzle at which the mean velocity profiles are self-similar also varied with Re. As a result, the jet attains self-similarity earlier as Re increases, i.e.,  $x/D = 25$  and  $10$  at Re equals 2000 and 6000, respectively.

The investigations done by Deo et al. (2008) on plane smooth contraction jets at Re equals 1500 to 16500 revealed that the inlet velocity profiles became flatter when Re increases. The highest values of  $u_{rms}/U_b$  (where  $U_b$  is the bulk exit velocity) decrease with the increase of Re. However, the centerline  $u_{rms}/U_b$  remains almost the same. It is observed that the potential core length, jet spread rates and the velocity decay decrease and the onset of self-similarity region moves downstream as Re increases. Furthermore, it is observed that the effect of Re is more considerable at  $Re < 10000$ . For instance, the spread rates, decreases from 0.14 to 0.10 as Re increases from 1500 to 10000. However, a further increase in Re to 16500 lead to only 10% reduction of the spread rate. In contrast, the asymptotic values of  $u_{rms}/U_{cl}$  increase from 0.16 to 0.23 when Re increases from 1500 to 16500. This disagrees with the observation by Namer & Otügen (1988) who reports that the asymptotic values decrease from 0.3 to 0.22 as Re increases from 1000 to 7000. Deo et al. (2008) hypothesize that this difference could be due to the lack of sidewalls in the experiments done by Namer & Otügen (1988).

The effects of  $Re$  from  $Re$  from 177 to 5142 on the characteristics of smooth contraction round jets were investigated by Kwon & Seo (2005). They detected that, similar to plane jets, increasing  $Re$  resulted in decreasing the spread rates and the potential core length. For instance, the spread rates reduced from 0.140 to 0.106 when  $Re$  increased from 1305 to 5142. However, the jet spread at  $Re = 177$  was negligible as the flow was laminar. Also, the decay rate was small at  $Re = 177$  and it increased to its asymptotic value of 0.182 when  $Re = 3208$ .

More recently, Mi et al. (2013) studied the flow properties of smooth contraction round jets at  $Re = 4000$  to 20000. It was seen that the length of the potential core was independent of  $Re$ . However, the velocity spread and decay rates decreased during an increase of  $Re$  up to value of 10000 and became  $Re$ -independent beyond  $Re = 10000$ . Mi et al. (2013) also detected that the centerline values of  $u_{rms}/U_{cl}$  in the self-similar region were higher at a lower value of  $Re$  and became asymptotic when  $Re$  is greater than 1000. However, in the near region, opposite trends were observed. The profiles of  $u_{rms}/U_{cl}$  showed faster growth and higher peak when the  $Re$  increased from 4050 to 6750. However, when  $Re$  was further increased to 20000, the growth rate decreased, and the peak value was smaller.

The studies conducted on round jets with  $Re = 177$  to 5142 by Kwon & Seo (2005) and on plane jets with  $Re = 1000$  to 7000 by Namer & Otugen (1988) also indicated that  $u_{rms}/U_{cl}$  grew faster as  $Re$  increased. Xu et al. (2013a) observed in pipe square jets that the centerline turbulence intensity grew slower when  $Re$  increased from 8000 to 50000. Therefore, it was found that even in the near region, two distinct regimes can be identified for the growth behavior of centerline turbulence based on  $Re$  and the nozzle type.

### 2.2.2. Steady Twin Jets

The flow behavior of multiple jets is more complex due to the interaction between neighboring single jets. A schematic of a twin round jet is given in Fig. 2.2. For twin jets, the following three distinct areas are identified: converging, merging and combined regions (Tanaka, 1970; Tanaka, 1974; Anderson and Spall, 2001). The converging region starts at the nozzle exit and extends to the point where the inner shear layers of the jets merge. This is denoted as MP (merging point) in Fig. 2.2.

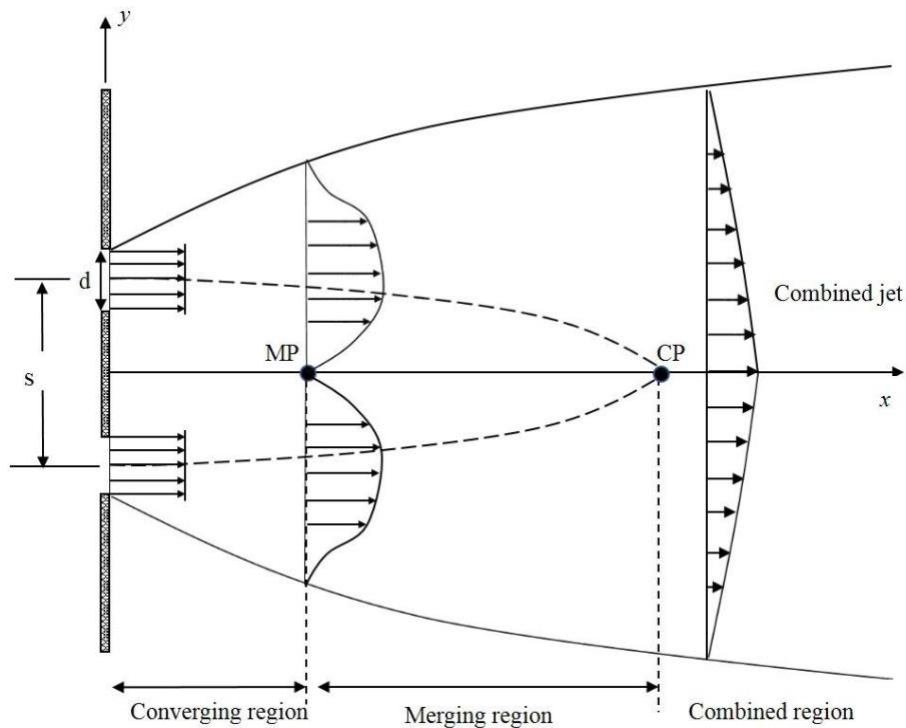


**Figure 2.2** Schematic of twin round jets. MP and CP are merging and combined points, respectively.

The asymmetry within the inner and outer shear layers results in an area of low pressure between the jets and consequently the jets are attracted toward each other and merge at the merging point. In the converging region the velocity on the symmetry plane of the jets might be negative, as has

been reported in plane twin jets research (Tanaka, 1970; Tanaka, 1974; Durve et al., 2012). The merging region is considered as a transition region between the merging point and the combined point. The combined point (CP), which is the onset of the mixed region, is defined as the point where the jets mixed completely to form a single jet. Therefore, this point indicates the onset of maximum velocity on the symmetry plane of the jets.

In contrast to single jets, twin jets are less studied in the literature. Most of the twin jet studies performed until now have focused on the effects of nozzle spacing (Tanaka, 1970; Tanaka, 1974; Lin & Sheu, 1990; Anderson & Spall, 2001; Harima et al., 2001; Harima et al., 2005; Durve et al., 2012). In addition, most of the studies have focused on twin plane jets. Despite of some qualitative similarities between round and plane twin jets, their flow behavior is fundamentally different. The reason is that twin round jets generate a three-dimensional flow where as the twin plane jets create a two-dimensional flow. Therefore, this section is divided into two sub-sections of twin plane jets and twin round jets.

#### **2.2.2.1. Twin Plane Jets**

Tanaka (1970) performed one of the earliest studies on twin jets. It was noticed that the jets were attracted to each other because of the low pressure between them. Also, in this region, the velocity was negative between the jets. Farther downstream, the velocity reached zero and then increased to positive values. The author introduced the following correlations for the streamwise location of the merging point ( $x_{MP}$ ), based on the results gathered from twin plane jets with  $8.5 \leq s/W \leq 26.3$ , where  $s/W$  is the nozzle spacing normalized by the nozzle width.

$$x_{MP}/W = 5.06(s/W)^{0.27} \quad s/W < 16 \quad (2.1)$$

$$x_{MP}/W = 0.667(s/W) \quad s/W > 16 \quad (2.2)$$

Also, the study revealed that the velocity distribution along the symmetry line was independent of  $Re$  for the range of 4290 to 8750.

In another study, Tanaka (1974) showed that the velocity profiles of the combined jet were like those of a single jet. Additionally, the combined jet spread linearly in the downstream and its width enlarged with the increase of distance between the nozzles. The results indicated that the velocity decay was greater for twin jets in comparison to a single jet. Also, the peak velocity along the symmetry line was independent of the  $Re$  number.

Lin & Sheu (1990) studied the flow fields of twin plane jets with  $s/W = 30$  and  $40$ . The results indicated that the merging point location was a linear function of the nozzle spacing:

$$x_{MP}/W = 0.48(s/W) + 8.98 \quad (2.3)$$

The mean velocity attained self-similarity in both the converging and combined regions. However, Reynolds shear stress and turbulent intensities revealed self-similar behaviors only in the combined region. They observed that, in both the converging and combined regions, the jets spread linearly, and the velocity decayed. However, the rates were higher in the converging region. Also, both the spread and decay rates were higher in comparison to a single plane jet.

Nasr & Lai (1997) showed that the installation of a side plate enhances the two-dimensionality of the jet flow field, which led to greater negative velocity and higher turbulence intensities in the converging region. They found that the streamwise mean velocity distributions of the jets were relatively independent of the Reynolds number ( $8300 \leq Re \leq 19300$ ).

Durve et al. (2012) numerically investigated the effects of inlet turbulence intensity and nozzle spacing on the locations of merging and combined points. It was determined that the Eq. (2.3) can predict the merging point of plane jets when  $s/W > 30$ , but not lower. It was indicated that for  $s/W > 30$ , the merging point is far from the jet inlet. Therefore, the jet's initial conditions do not affect its position. They suggested equations for merging and combined points as a function of nozzle spacing and inlet turbulent intensity according to their numerical studies and previous experimental data from the literature.

$$x_{MP}/W = 0.721(s/W) + 2.06(u_{rms}) - 2.453 \quad (2.4)$$

$$x_{CP}/W = 1.231(s/W) + 2.06(u_{rms}) - 2.453 \quad (2.5)$$

Wang et al. (2016) studied twin plane jets with nozzle spacing of  $s/W = 3$  and  $Re = 9100$  using Particle Image Velocimetry (PIV). Strong velocity fluctuations were detected right after the merging point which was concluded that the main momentum transfer occurred in the merging region. They also observed that the jets diverged immediately after hitting each other but rejoined again a few times before the jets fully merged.

#### **2.2.2.2. Twin Round Jets**

Okamoto et al. (1985) studied the effects of nozzle spacing of  $s/D = 5$  and 8, where  $D$  is the diameter, on the velocity field of twin round jets at a  $Re$  of 230000. Their results indicated a faster shift in the position of the peak velocity from the nozzle centerline to the line of symmetry of the jets at  $x/D = 5$ . From the velocity contours it was shown that initially the jets merged in the form of an ellipse. However, they became close to a round jet farther downstream, i.e., at  $x/D = 58$  for a twin jet with  $s/D = 5$ . The spread of the jets was slightly larger than that of a single jet in

the inner shear layer, while in the outer shear layer the single jet spread faster in comparison to the twin jets. However, the spread rates of the single and twin jets were the same in the plane passing through the nozzle center.

The effects of nozzle spacing,  $s/D = 2, 4$  and  $8$ , at a  $Re = 25000$  were explored by Harima et al. (2001) and Harima et al. (2005). The results revealed that an increase of  $s/D$  from  $2$  to  $4$  and then  $8$ , shifted the combined points from  $x/D = 25$  to  $52$  and then  $90$ , respectively. Also, the locations of maximum turbulence intensity moved to downstream and the maximum value decreased.

Vouros & Panidis (2008) investigated the influence of the Reynolds number on the behavior of two round jets with different diameters. They set a  $Re$  of  $5500$  for the primary jet and a  $Re$  of  $1200$  then  $1800$  for the secondary jet. In both cases, the secondary jet was absorbed by the primary jet. However, the secondary jet disappeared faster when the  $Re$  was lower. In addition, they found higher values of the mean and turbulent quantities and jet spread for the configuration with the secondary flow at the higher  $Re$  value.

Zang & New (2015) performed PIV to investigate the effects of nozzle spacing on the vortical structures in twin round jets. When the distance of the center of the nozzles were  $1.5$  to  $2$  diameters, they observed that the different-signed vortices in the inner shear layers were staggered with each other, acting like the wake vortices behind a bluff body. However, for  $s/D = 3$ , jets behaved like two separate single jets due to less interaction between the vortices.

### 2.3. Pulsatile Jets

Pulsatile jets are not investigated much in the literature except for a few works. In theory, an important parameter that defines a single jet vortex development is the formation number or formation time. This parameter introduced by Gharib et al. (1998) is the ratio of length to diameter of the ejected fluid, i.e.,  $L/D$ . Gharib et al. investigated the formation time for vortex ring generation through impulsively initiated jets. Experiments were conducted under similar conditions with small variations in the settings to generate the jets and subsequent vortices. The goal of this study was to find a limiting process in vortex growth. They defined this limiting factor as a ratio between the piston stroke and the diameter,  $L/D$ . After a series of experiments, they observed that the vortex ring stops growing after a  $L/D = 4$ . Passing this number, the vortex stops growing and they instead observed a distinct trailing jet. Furthermore, it was observed that the change in the boundary conditions results in a decrease in the value of the formation time and an increase of the Reynolds number. Also, the removal of the impulsive motion of the piston results in an increase of the formation number.

Dabiri & Gharib (2005) investigated a time-varying nozzle exit diameter to mimic biological systems. They found that temporal increase in jet exit diameter does not change the vortex-limiting formation time from the constant-diameter. Also, they showed that these temporal increases in jet exit diameter during the formation of the leading vortex, increase thrust, and impulse generated by the system. They concluded that the strategy of enlarging the orifice or nozzle during early formation of the vortex ring is in favor of the biological systems with rapid impulse generation during jet initiation.

Chetina (2015) investigated flexible orifices of a pulsatile flow. She studied orifice geometries referred to as no-clip, middle-clip, and side-clip configurations. The flow was

generated through a piston-cylinder setup and time-resolved PIV was used for flow measurements. It was concluded that the highest energy consumption was associated to the middle and side-clip configurations. Although the side-clip configuration was discovered to be dominated by higher Reynolds shear stresses, she concluded that the longer presence of stresses, in combination with higher energy fluctuations, due to the turbulent kinetic energy could produce more blood damage in the middle-clip configuration.

## **2.4. Objective of the Present Study**

Although there are many studies regarding single free jets, there are not many when the two jets are close (small  $s/W$ ). Also, most of the studies do not consider pulsatile flow conditions and are focused on gases and tend to cover the self-similar region. Therefore, in this study, the purpose is to enrich the field of research covering the near region and merging region of pulsatile jets. In particular, the intent is to investigate the effect of different orifice configurations after simulated ETER on the flow using Time-Resolved PIV (TR-PIV). This will help to further develop the method used in the ETER technique. For this purpose, advanced techniques, such as Proper Orthogonal Decomposition (POD), and Continuous Wavelet Transform (CWT) are used to characterize the dynamics of the interaction of two jets produced downstream of a double-orifice configuration. This is a fundamental study which simplifies the system to reflect the basic processes and capture the essence of jet interactions following ETER.

## **3. Methodology**

Experiments were performed previously by Chtchetinina (2013) in order to analyze the dynamics of liquid jet interactions generated from a pulsatile fluid flow to mimic the flow in the left ventricle. For completeness, this chapter is thus devoted to the description of the experimental setup and the procedure, along with information on the preliminary setup calibration and PIV measurements. Then, data post-processing methods are presented in the next chapter. To demonstrate the accuracy of the experimental setup, it is compared with the published results of a single liquid jet in the literature.

### **3.1. Experimental Apparatus**

The setup consists of a small diameter piston-cylinder device connected to a large transparent Plexiglas water tank of the size  $30.5 \times 94 \times 63$  cm. The pulsatile flow is driven by a piston-cylinder using a pump control system (SuperPump pump by ViVitro Systems Inc.). A 32 mm circular nozzle with a healthy or sutured model of a mitral valve is attached to the end of the piston-cylinder where the flow emerges into the water tank. The study investigates the dynamics of jet(s) emerging from different MV configurations which mimic normal MV, double-orifice MV repaired with suture in the middle, as well as double-orifice MV repaired with suture on the side. The schematic of the setup and the valves are given in Fig. 3.1.

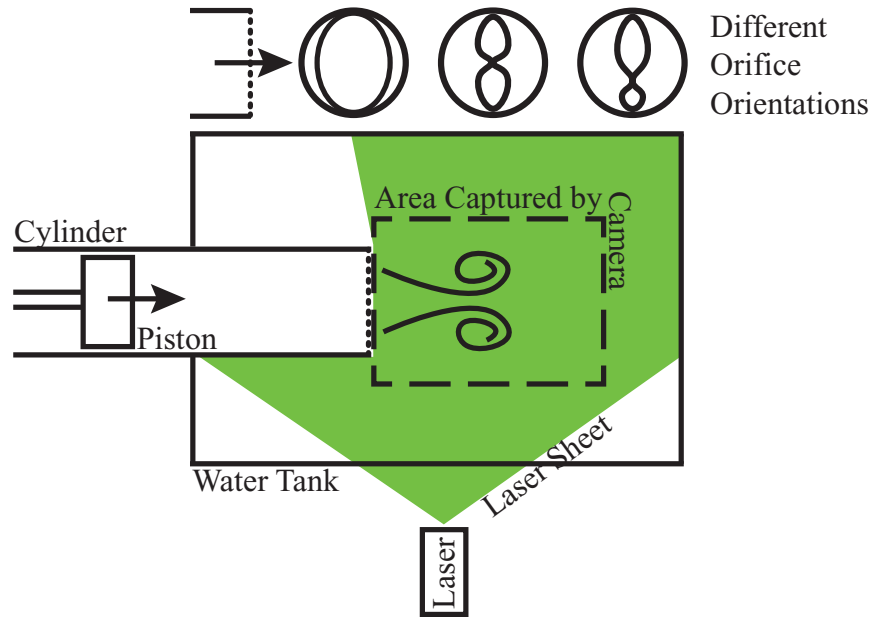


**Figure 3.1** Top view schematic of the experimental setup and orifice configurations. The dashed line displays area of investigation captured by the camera

### 3.2. Experimental Procedure

In order to generate the liquid jet from a pulsatile flow and study its dynamics, the piston movement generated by the pump is controlled by a function generator with a custom user interface created in LabView software. The pump is then provided with a ramp function signal to animate the different stroke piston which is close fitted in the bore of a 35.5 cm long and 32 mm inner diameter cylinder. Three types of orifice configuration as described previously, is then attached at the exit of the cylinder. The distance between the piston face and the cylinder exit at maximum stroke is sufficiently adequate to disregard the vortex generated by the piston head (Allen & Auvity, 2002). The Plexiglas tank is filled with room temperature water/particle mixture and the cylinder is submerged. The dual frame CCD camera is located below the tank at a distance of 15.6 cm, directly underneath the cylinder exit, normal to the exit plane and captures the dashed line in Fig 3.1. The

camera is connected to a synchronizer to link it to the laser, the function generator, and the computer with the PIV software. A double-pulsed Nd-YLF laser is used to illuminate the working flow. The laser sheet is produced through sheet-forming optics attached on the head of an articulated laser arm, and it is approximately 1 mm thick. The laser sheet is aligned with the center of the MV's orifices, crossing both orifices in the DO MV configuration case and along the axis of vortex ring motion. The recording frequency is 350 Hz and the recording time for each experiment is one second.

### **3.3. Flow Velocity Measurement**

Particle Image Velocimetry (PIV) technique is used to visualize the flow. This technique allows non-intrusive, indirect velocity measurement which is possible even on a large segment of a flow field. Therefore, it covers the entire area of interest (AOI) in this study.

The underlying principles of PIV are straight forward. The distance traveled by an object divided by the time elapsed indicates the velocity of the object. The main components of the PIV setup are a charge-coupled device (CCD) or complementary metal-oxide-semiconductor (CMOS) camera, a laser, and a flow seeded with tracer particles.

The image analysis is a statistical method, using a cross-correlation technique based on the examination of a double frame. Seeded tracer particles in the flow of interest are illuminated with a double-pulsed laser sheet produced by a laser with attached sheet-optics. These particles are considered as a signal and are captured at two instances with a known time interval of  $\Delta t$ . Then, the AOI is reflected onto the sensor array of the CCD or CMOS camera through the imaging optics. Each of the two frames of the same image are then divided into small localized subsections, called

interrogation areas (IA) in order to process these signals. These IAs are then cross-correlated with each other to detect the common linear spatial movement of groups of particles,  $\Delta x$ , while producing signal peaks that reflect particle locations. The motion of each group is then translated into a velocity vector. The cross-correlation process is outlined in Fig. 3.2.

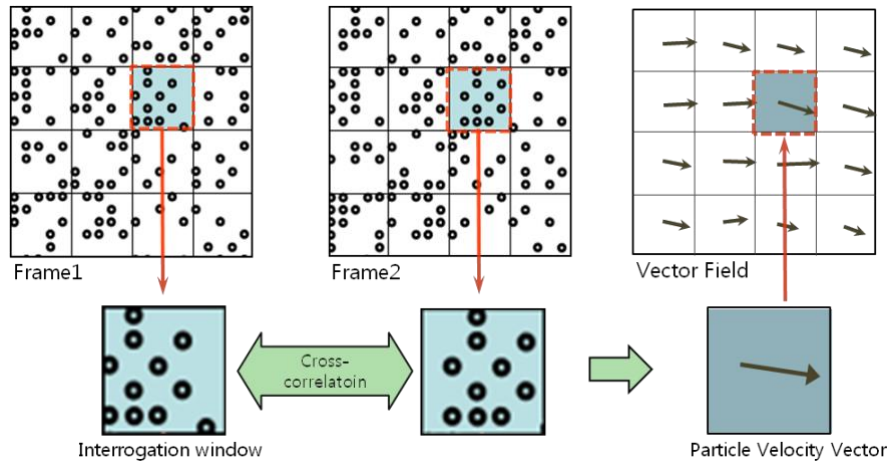


**Figure 3.2** Cross-correlation process (Choi et al., 2011)

A velocity vector map is produced by applying the cross-correlation to all the IAs over the entire AOI. These vector maps are then used for further post processing of the flow of interest such as streamlines, vorticity, and dissipation of energy. Figure 3.3 shows a clear visualization of the measuring principles of PIV. In this work, DaVis 7.2 software from LaVision was used to control the PIV system and data collection. This software allows synchronization of system devices. The data collected from the high-speed camera were images in *.im7* format. These images contain tracer particle locations, and they were then processed using cross-correlation to calculate vector fields. Data was then transferred into DATA file format *.dat*, and further calculations were done with MATLAB 2018a.

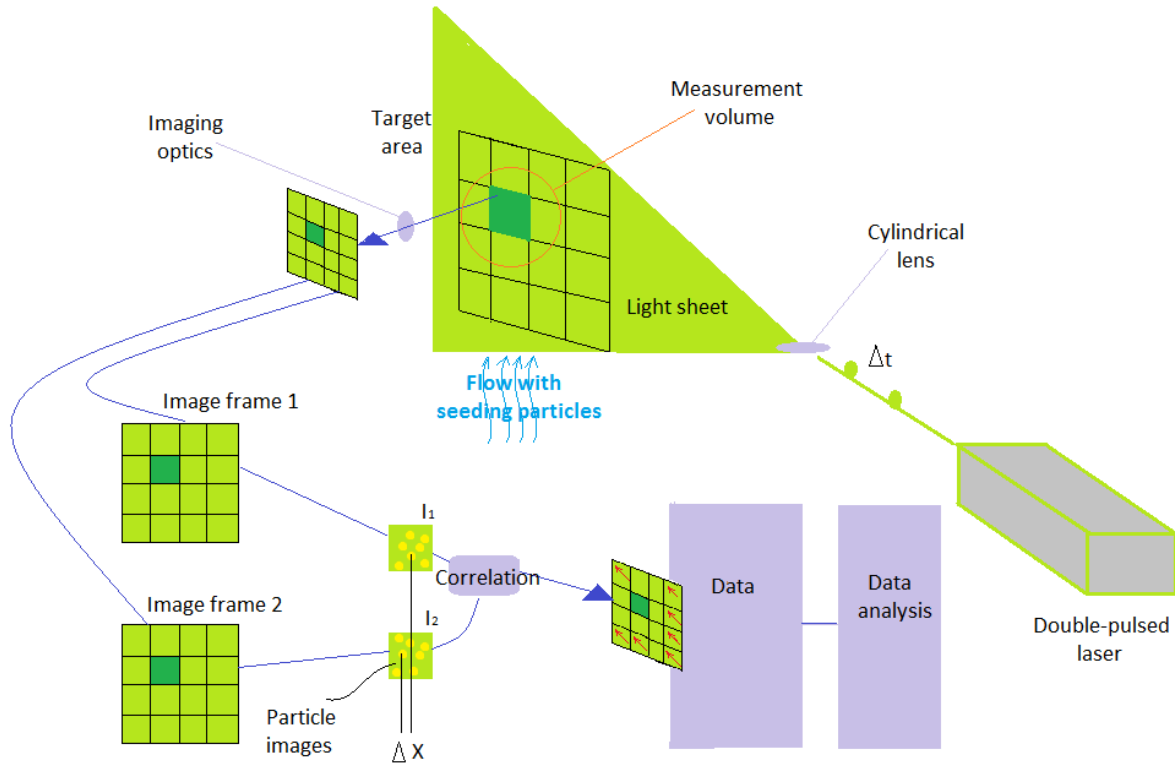


**Figure 3.3** Schematic depicting a typical PIV system ([http://home.zcu.cz/~rcermak/opvk\\_htt/VY\\_01\\_02.pdf](http://home.zcu.cz/~rcermak/opvk_htt/VY_01_02.pdf))

Several PIV tests with time delays between the two laser pulses varying from  $100 \mu\text{s}$  to  $1000 \mu\text{s}$  made it clear that  $\Delta t = 900 \mu\text{s}$  is suitable for all sets considered in this investigation. The process of selecting for the maximum  $\Delta t$  is further explained in detail later in the setup calibration section. The working fluid is water, and is seeded with  $10 \mu\text{m}$ ,  $d_p$ , hollow silver-coated glass spheres with a density,  $\rho_p$ , of  $1.4 \text{ g cm}^{-3}$ . The Stokes number,  $S_{tk}$ , is calculated in order to evaluate the response of the particle inertia to viscous drag in the flow. For  $S_{tk}$  above unity, the tracer particle will detach from the flow in the event of a sudden velocity change, whereas a smaller number indicates that particles are able to follow the streamlines of the flow (Melling 1997). The Stokes number is a ratio of the particle relaxation time,  $\tau_p$ , divided by the characteristic time scale of the fluid,  $\tau_f$ :

$$S_{tk} = \frac{\tau_p}{\tau_f} \quad (3.1)$$

where particle relaxation time is expressed as

$$\tau_f = \frac{\rho_p d_p^2}{18\mu} \quad (3.2)$$

In this equation  $\rho_p$  is the particle density,  $d_p$  is the particle diameter, and  $\mu$  is the viscosity of the working fluid, 1.002 mPa · s. The characteristic time scale of the fluid flow is

$$\tau_p = \frac{L_f}{U_f} \quad (3.3)$$

$L_f$  here is the flow characteristic length, 43 mm, which is taken as the minimum piston stroke.  $U_f$  is the fluid characteristic velocity, 176.47 mm/s, used as the minimum exit velocity, and assumed to be equal to the piston velocity. The number was much less than unity, showing high particle responsiveness to the experimental flow fluctuations. Seeding particles properties used in this work are listed in Table 3.1.

**Table 3.1** Selected seeding particle properties

Seeding particles	S-HGS Silver-coated hollow glass spheres
Mean particle size	10 $\mu\text{m}$
Particle shape	spherical
Density	1.4 g/cm <sup>3</sup>
Material	Borosilicate glass

The range of the Reynolds numbers based on the average velocity at the exit can be found in Table 3.2.

**Table 3.2** Average Reynolds number for different configurations

Average Reynolds Number for Different $L/D$	Single-orifice	Symmetric double-orifice	Asymmetric double-orifice
$L/D=1.5$	2733	9842	7105
$L/D=1.9$	3751	11224	10143
$L/D=2.5$	3842	12887	10692

### 3.4. Setup Calibration and Validation

In order to evaluate the setup performance and find the optimal parameters for the PIV measurement, a series of calibrating experiments are performed. To produce a set of single jet vortex rings, a 7.94 mm nozzle is attached to the cylinder exit. Later on, the results are analyzed and compared with previous studies (Gharib et al., 1998).

After assembling all components of the setup, the PIV system is calibrated to the appropriate scale. A high-precision calibration plate is used for this purpose with an accuracy of  $\pm 0.02$  mm tolerance dot pattern. The plate is aligned with the camera at the level of the laser sheet. Then to set the mm per pixel scale, or the calibrating scale  $\alpha$ , an image is taken. Then, this step is finalized by defining the distance in mm between the two points of the plate that are displayed on the screen of the computer.

The selection of the seeds mainly depends on the resolution of the image. When the particle image is too small, an issue known as ‘peak locking’ will happen (Raffel et al., 2007). In peak locking, displacement evaluated from cross-correlation is biased towards integer values. The presence of peak locking effect for this work experiment is evaluated using a probability density function (PDF) of both axial,  $V_x$ , and transverse velocities,  $V_y$ . PDF was calculated by using DaVis software on the whole vector field. 216 bins and one tenth pixel slot resolution from one of the samples were used. The value of the effect was 0.128, which is much less than unity. This indicates a negligible peak locking level (LaVision GmbH, 2009).

As mentioned previously, the time interval between the two laser pulses was set at 900  $\mu$ s during the system calibration and was kept throughout all of the experiment. This value corresponds to

less than one fourth of the interrogation window size (Anderson & Spall, 2001). The value is calculated with the following equation:

$$\Delta t = \frac{\Delta x_{mm}}{V_{max}} \quad (3.4)$$

where  $V_{max}$  is the maximum flow velocity and  $\Delta x_{mm}$  is the maximum displacement allowed to achieve the  $\frac{1}{4}$  interrogation window size in millimeters.  $\Delta x_{mm}$  is found from the following equation:

$$\Delta x_{mm} = \alpha \Delta x_{pix} \quad (3.5)$$

In this equation,  $\alpha$  is the calibrated scale factor and  $\Delta x_{pix}$  is the maximum displacement allowed to fulfill the one fourth of the interrogation window size in pixels. The allowed pixel displacement is found by dividing the IA by 4. In this particular work, IA is  $32 \times 32$  pixels, which provides an allowable pixel displacement of 8. The calibrated scale factor is  $\alpha = 0.078$  mm/pixel. The exit velocity from the nozzle,  $V_p$ , is taken as the maximum flow velocity. It is calculated from the known maximum piston velocity,  $V_p = 48.212$  mm/s, through the volume flow rate-velocity relation,

$$Q_p = Q_{exit} \quad (3.6)$$

$$A_p V_p = A_{exit} V_{exit} \quad (3.7)$$

$$r_p^2 V_p = r_{exit}^2 V_{exit} \quad (3.8)$$

$$V_{exit} = \frac{r_p^2 V_p}{r_{exit}^2} \quad (3.9)$$

In these equations  $Q_p$  and  $Q_{exit}$ ,  $A_p$  and  $A_{exit}$ ,  $r_p$  and  $r_{exit}$  are volume flow rate, area, radius of the piston, and the nozzle exit respectively. Consequently, the maximum allowable  $\Delta t$  of  $1500 \mu s$

is obtained. However, for the experiment, the value of 900  $\mu\text{s}$  was used. That is because it satisfied the  $\frac{1}{4}$  interrogation window rule. Furthermore, it provided a fair quality vector field for the entire tested range of the piston velocities. Later, these calculations are repeated for the actual experiment. The parameters used in the actual experimental PIV tests are outlined in Table 3.3.

**Table 3.3** Parameters used in the PIV measurement

<b>Number of images</b>	350
<b>Recording rate</b>	350 Hz
<b><math>\Delta t</math></b>	900 $\mu\text{s}$
<b>Recording duration</b>	1 s
<b>Camera adjusted chip size</b>	1632 $\times$ 1120 pixels
<b>Picture size</b>	1632 $\times$ 1120 pixels
<b>Scale factor</b>	0.078 mm/pixel
<b>Seeding particles</b>	10 $\mu\text{s}$ silver-coated hollow borosilicate glass spheres with a density of 1.4 g/cm <sup>3</sup>

Before the post processing, a median filter was applied to substitute the noisy velocity vector with the median of the neighbors.

### 3.5. Continuous Wavelet Transform

Traditionally, turbulent statistical signals were often analyzed by Fourier transforms. As a result, important temporal information was lost due to the non-local nature of the Fourier modes. However, Wavelet Transform (WT) has the ability to demonstrate frequencies with their associated temporal information. On the other hand, WT ability to examine the signal simultaneously in both time and frequency is different from the traditional short-time Fourier transform (STFT). STFT gets frequency components of local time intervals of fixed duration. However, to analyze signals that contain non-periodic and fast transient features (i.e. high

frequency content for short duration), STFT analysis is not useful. Therefore, CWT is the best method to investigate a turbulent velocity signal in this work.

Wavelet transform analysis uses functions known as wavelets. Wavelets are used to transform the signal under investigation to another more useful representation. Mathematically speaking, the wavelet transform could be interpreted as a convolution of the signal with a wavelet function. Figure 3.4 shows a schematic of the wavelet transform which quantifies the local matching of the wavelet and the signal. A wavelet could be manipulated by moving it to various locations on the signal and by stretching or squeezing it to find the matching scale. If the wavelet matches the shape of the signal at a specific scale and location, then a large transform value is obtained. Otherwise, a low transform value is achieved. The transform is computed at various locations of the signal as well as for various scales of the wavelet. Therefore, it fills up the transform plane. The schematic of this transform can be found in Fig. 3.4.

Morlet wavelet which is a complex wavelet is used in a variety of fluid mechanic research and is the chosen wavelet in this work. It has the following equation.

$$\Psi\left(\frac{t-b}{a}\right) = \pi^{-\frac{1}{4}} e^{2i\pi f_0 \left[\frac{t-b}{a}\right]} - e^{-\frac{1}{2}[(2i\pi f_0)^2/a]^2} \quad (3.10)$$

where  $f_0 = 0.849$  is the central frequency of the mother wavelet. The parameters  $a$  and  $b$  are used as a means to change the scale and the location of the wavelet respectively.

Now we can calculate the continuous wavelet transform (CWT).

$$T(a, b) = a^{-\frac{1}{2}} \int_{-\infty}^{+\infty} u(t) \Psi^*\left(\frac{t-b}{a}\right) dt \quad (3.11)$$

Where the ‘\*’ indicates that the complex conjugate of the wavelet function is used in the transform.

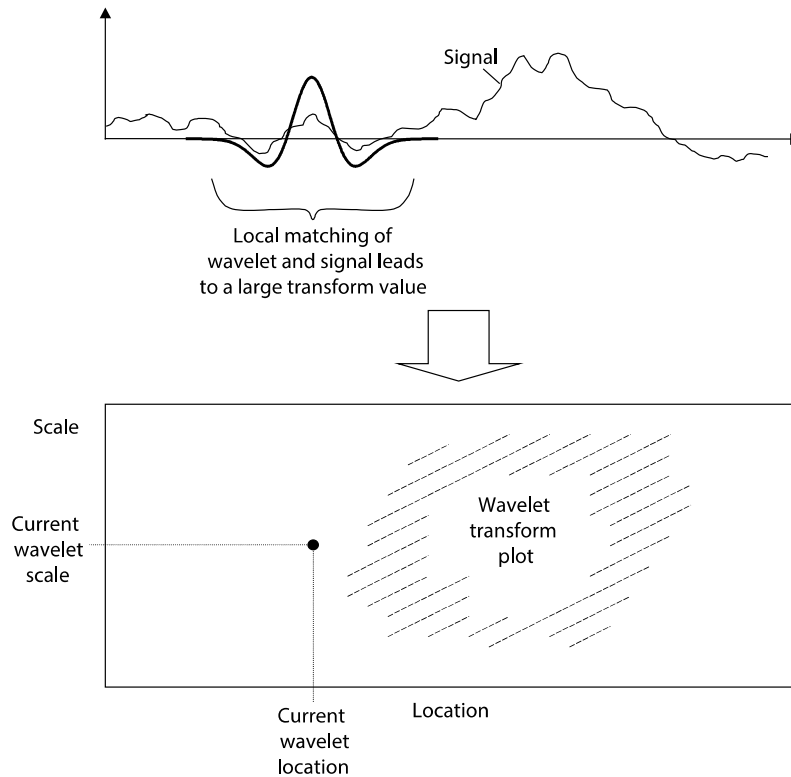


**Figure 3.4** Schematic of continuous wavelet transform and local matching of the wavelet and the signal (Addison, 2017)

### 3.6. Viscous Energy Dissipation

In the absence of energy dissipation during fluid motion, kinetic energy and potential energy can be exchanged but the change in the sum of kinetic and potential energy is equal to the work done to the system. However, viscous effects result in an irreversible conversion of mechanical energy into internal energy or heat.

Turbulent flow consists of eddies of various size range, and this range increases with increasing Reynolds number. The kinetic energy drops from large to small eddies by interaction forces between the eddies. Due to viscous forces, the energy of these eddies dissipates into heat at a very

small scale (Richardson, 1992). Therefore, energy dissipation rate is a parameter that determines the amount of energy lost by the viscous forces in the turbulent flow.

Turbulent flow is a complex phenomenon, which is highly unpredictable. However, turbulence has several common characteristics such as nonlinearity, vorticity, diffusivity and finally energy dissipation. Based on these features, turbulence can be considered as a dissipative flow state characterized by nonlinear fluctuating three-dimensional vorticity (Kundu et al., 2012).

The dissipation property of the turbulent flow is responsible for the conversion of kinetic energy into heat due to large velocity gradients created by eddies of various scales. To overcome this loss, external energy is required, i.e., the human heart needs to work harder.

Viscous Energy Dissipation Rate (VEDR) is a measure of the efficiency of the flow and it indicates how well the flow conserves its kinetic energy. The quantity of VEDR is larger when the velocity gradients are greater, i.e., in jets and shear layers.

VEDR in an incompressible model could be calculated as it is done by Pedrizzetti & Domenichini (2015), Stugaard et al. (2018) and Di Labbio et al. (2019).

$$VEDR = \frac{\mu}{2} \int_A \left( \sum_{\forall i,j} \left( \frac{\partial u_i}{\partial x_j} + \frac{\partial u_j}{\partial x_i} \right)^2 \right) dA \quad (3.12)$$

where  $\mu$  is the dynamic viscosity. For a 2D flow as the work in this research, Viscous Energy Dissipation (VED) can be calculated as below.

$$VED = \mu \iiint \left( 2 \left( \frac{\partial u}{\partial x} \right)^2 + 2 \left( \frac{\partial v}{\partial y} \right)^2 + \left( \frac{\partial u}{\partial y} + \frac{\partial v}{\partial x} \right)^2 \right) dx dy dt \quad (3.13)$$

In this work Empirical Mode Decomposition (EMD) is used to smoothen some of the signals for better visualization. EMD is introduced by Huang et al. (1998). It is a data-driven, adaptive signal

processing method which works best for analyzing non-stationary and nonlinear signals, like the ones in this research. This algorithm decomposes a signal into a sum of Intrinsic Mode Functions (IMF), where each IMF represents a simple oscillatory function. By applying the EMD algorithm we decompose a signal  $u(t)$  into a set of IMF functions in decreasing order of oscillatory behavior and with a residue.

$$u(t) = IMF_1(t) + IMF_2(t) + \dots + IMF_n(t) + R(t) \quad (3.14)$$

The first IMF component captures the oscillations with higher frequencies. EMD can be easily applied on a signal in order to reconstruct it without its first IMF. Figure 3.5 shows how removing the first IMF is smoothing the signals.

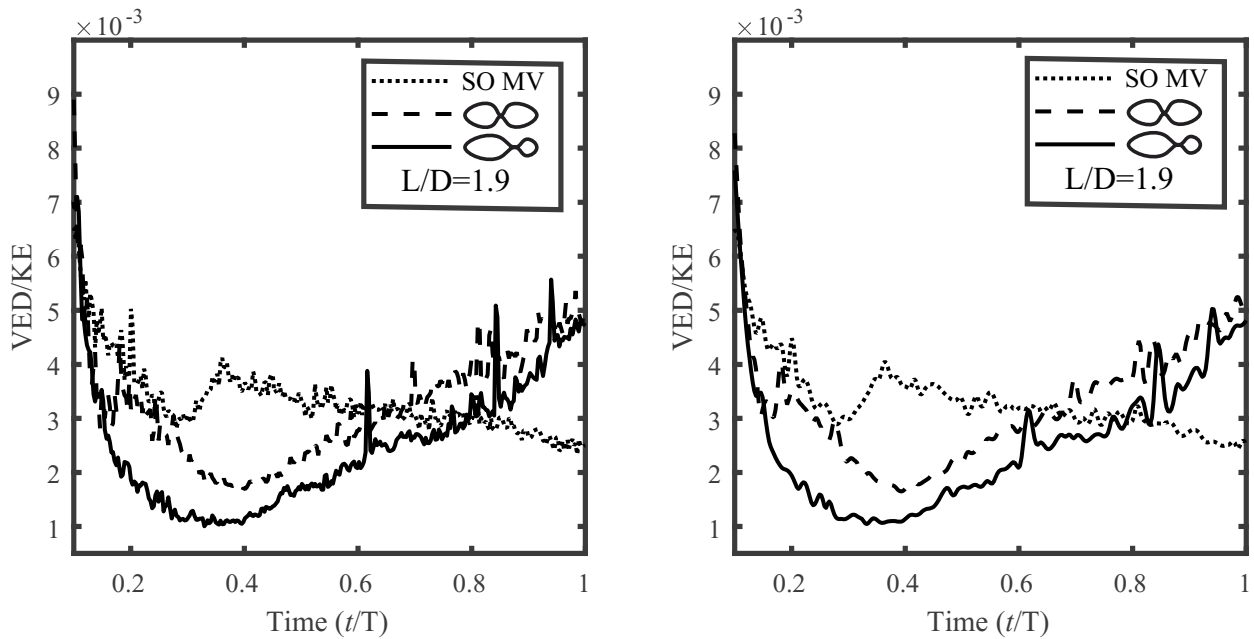


**Figure 3.5** Ratio of viscous energy dissipation and kinetic energy. Original signals are displayed on the left. First IMF is subtracted from the signals on the right

### 3.7. Proper Orthogonal Decomposition

In this work, POD is applied on data obtained from 2D time-resolved PIV to understand the structure of the flow before and after ETER.

The proper orthogonal decomposition was originally developed by Pearson (1901) about 100 years ago for graphical analyses. The method further developed by Hotelling (1933), Karhunen (1946) and Loeve (1955). It was introduced to in the context of fluid mechanics first by Lumley in 1967. The most striking feature in POD is its optimality. It provides the most efficient way of capturing the dominant components of the flow with usually a few modes (Liang et al., 2002). POD can also be used for noise cancelling proposes and dimension reduction purposes.

POD has applications in a variety of fields including:

- Transient thermal analysis (Bialecki, 2005)
- Description of turbulent fluid flows (Holmes et al., 1993)
- Structural dynamics (Kerschen., 2007)
- Signal processing and control theory (Ly & Tran, 2001)
- Damage detection (Ruotolo & Surace, 1999)
- Human face recognition (Sirovich & Kirby, 1987)
- Unsteady aerodynamics (Tang et al., 2001)

Snapshot POD is introduced by Sirovich in 1987 and it is widely used as a means to investigate the flow structure. To apply POD, all the  $n$  snapshots of  $m$  points are arranged in a single matrix,  $\mathbf{X}$ , as below.

$$\mathbf{X} = \begin{bmatrix} | & | & & | \\ \mathbf{x}_1 & \mathbf{x}_2 & \dots & \mathbf{x}_n \\ | & | & & | \end{bmatrix} \quad \text{where} \quad \mathbf{x}_k = \begin{bmatrix} u_{1k} \\ \vdots \\ u_{mk} \\ v_{1k} \\ \vdots \\ v_{mk} \end{bmatrix} \quad (3.15)$$

Mathematically speaking, POD divides the  $\mathbf{X}$  matrix into a linear combination of spatial and temporal modes in a way that spatial modes are orthogonal. To find these modes, we first need to calculate the correlation matrix:

$$\mathbf{C} = \mathbf{X}^T \mathbf{X} \quad (3.16)$$

The next step is to calculate eigenvalues and eigenvectors of the correlation matrix from the below equation and then sort the eigenvalues by their magnitude.

$$\mathbf{CQ} = \mathbf{QA} \quad (3.17)$$

As a result, we have a matrix  $\mathbf{Q}$  of eigenvectors in each column sorted by correspondent eigenvalues in a diagonal matrix  $\mathbf{A}$  of eigenvalues. In the end, spatial matrix  $\mathbf{\Phi}$  and temporal matrix  $\mathbf{B}$ , are calculated as below:

$$\mathbf{\Phi} = \mathbf{XQ} \mathbf{A}^{-\frac{1}{2}} \quad (3.18)$$

$$\mathbf{B} = \mathbf{\Phi}^T \mathbf{X} \quad (3.19)$$

where each column of  $\mathbf{\Phi}$  contains a spatial mode sorted based on their energy, i.e., the first mode has the highest energy. Also, each row of  $\mathbf{B}$  contains a temporal mode associated with a column of matrix  $\mathbf{\Phi}$ . The data transformation in POD is linear (Perrin et al., 2007), therefore we can reconstruct the matrix  $\mathbf{X}$  with linear combination of spatial and temporal modes, i.e.,

$$\mathbf{X} = \mathbf{\Phi} \mathbf{B} \quad (3.20)$$

It is clear that each diagonal element of the correlation matrix,  $\mathbf{C}$ , corresponds to the kinetic energy of velocity fields. The summary of the MATLAB code for calculating the POD can be found in the Appendix.

## 4. Results

The purpose of this chapter is to investigate the results of the *in vitro* experiments, both before and after simulating ETER. High turbulence in the LV causes damage to blood cells. Therefore, time frequency analysis using wavelet transform is used to identify turbulence in the flow in the presence of different MV configurations. Also, when there is excessive energy losses in LV, the heart requires to work harder to keep a normal pumping function. Viscous energy dissipation is a good indication of energy loss and it is investigated in this work to compare between the different cases and more specifically between the two edge-to-edge repair configurations. At the end of the chapter, POD is applied to generate a reduced order model and to identify the most significant coherent structures in the flow field.

### 4.1. Vortex Path in Single Configuration

The purpose of this section is to validate the results in the case of single orifice. The core vortex path in SO MV is measured using  $\Gamma_2$  vortex criterion.  $\Gamma_2$  criterion is introduced by Graftieaux et al. (2001) to characterize the locations of the center and the boundary of the vortex.

In Fig. 4.1,  $x$ -position of the upper vortex is plotted in time of the experiment. The slope of the lines in Fig. 4.1 shows the velocity of the vortex in the  $x$ -direction. It can be seen that vortices have almost a constant velocity in  $x$ -direction. It is also interesting that the ratio of these velocities is almost the same as the formation time ratio. The results are displayed in the Table 4.1 and they are in agreement with Gharib et al. (1998) findings. Table 4.1 shows streamwise velocity of the vortex in SO MV almost linearly changes by increase in formation time in duration of this experiment. Therefore, the velocity of the vortex can be predicted in these experiments by knowing the formation time. The noises are removed from the path using continuous wavelet transform

(complex Morlet wavelet). First, the  $x$ -position signal in time is obtained from the path. Then the signal is decomposed to a straight line (i.e., translational velocity of the vortex ring) and the rest of fluctuations. Since the straight line does not have any frequency, the wavelet transform is applied on the fluctuations part only. Then assuming the velocity in direction of the jet,  $x$ , is always positive, frequencies more than 20 are removed by using inverse wavelet transform. It is observed that most of the oscillations in  $x$ -position and  $y$ -position signals have the frequency of 7 to 20.

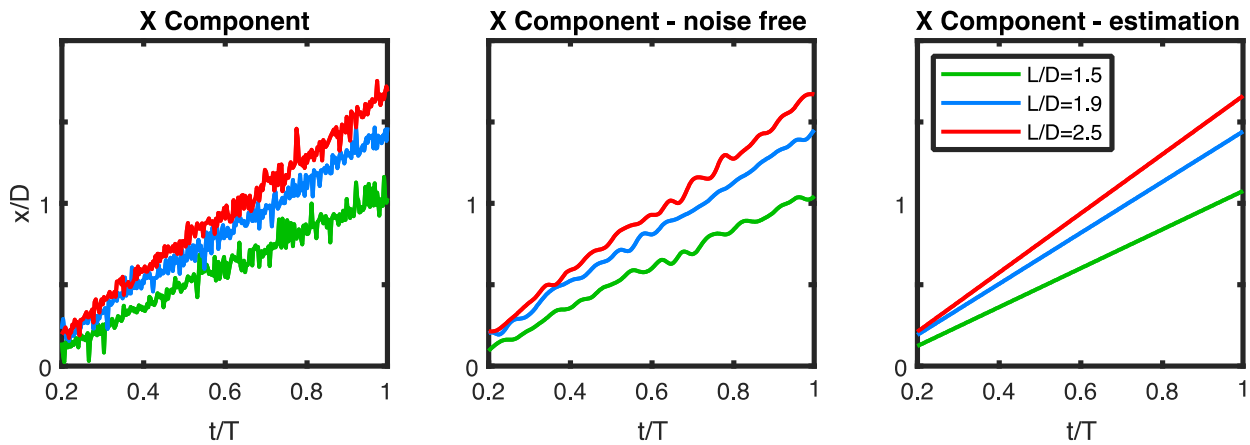


**Figure 4.1** X-Positions of upper vortices in SO MV are plotted. In the middle panel the noises (frequencies more than 20) are removed using morlet wavelet in wavelet transform. The right panel is a linear estimation.

**Table 4.1** Comparison of formation time ratio and core velocity ratio of the upper vortex in SO configuration. The right column is the difference between the  $L/D$  ratio and the velocity ratio.

$L/D$ Ratio	Velocity Ratio	Difference
$1.9/1.5 = 1.27$	$31.36/23.90 = 1.31$	3.2 %
$2.5/1.5 = 1.67$	$36.36/23.90 = 1.52$	9.0 %
$2.5/1.9 = 1.32$	$36.36/31.36 = 1.16$	12 %

## 4.2. Flow Visualization

Figures 4.2 and 4.3 display examples of velocity and vorticity snapshots for three different MV configurations and three formation times. Figure 4.2 shows the development of the single-orifice

configuration in three snapshots. It can be noticed that a single-orifice configuration leads to a vortex ring formation, and the vorticity which is an indication of vortex strength is enlarged according to the formation time.

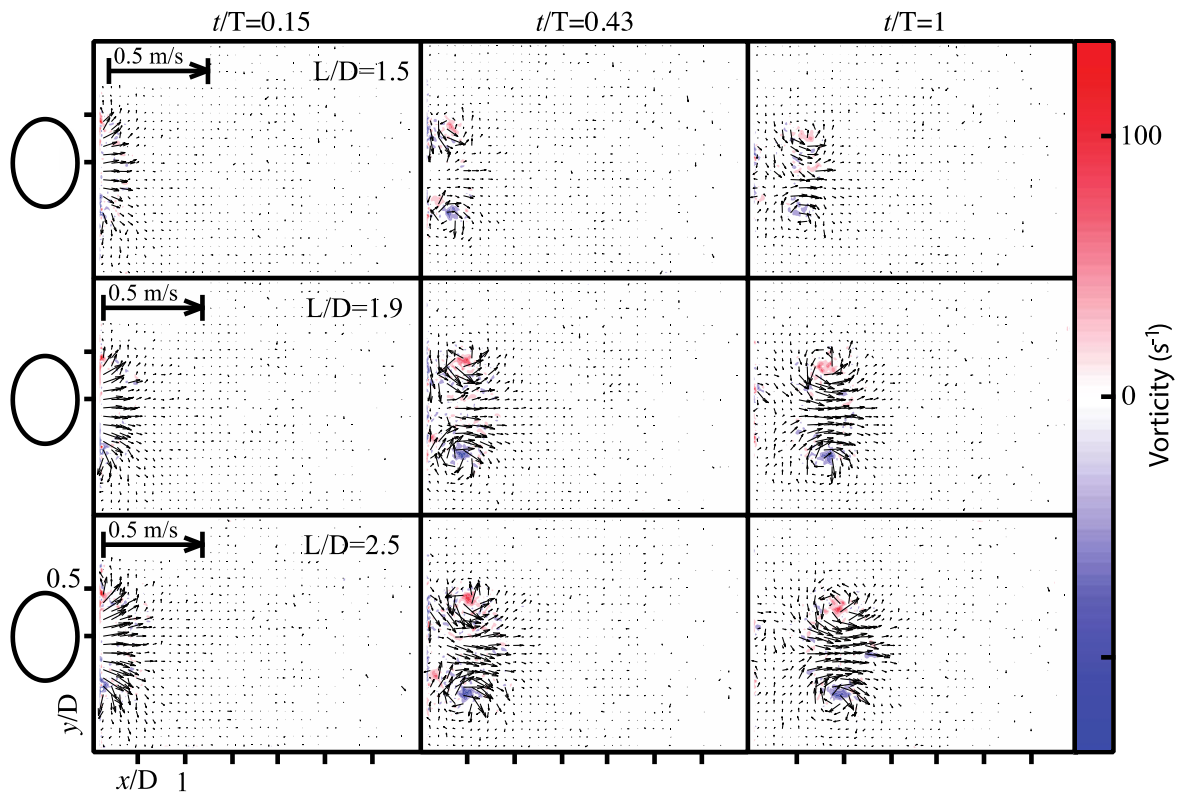


**Figure 4.2** Three formation time of a single-orifice configuration at different instances are presented.  $L/D$  from top to bottom is 1.5, 1.9 and 2.5

Also, the vortex ring travels faster and the vorticity is greater when the formation time is increased. However, there is no trailing jet behind the vortices which indicates the leading vortex has not reached its maximum strength. One can say the vortex in the single-orifice configuration well preserves the energy of the jet, as the magnitude of velocity vectors remains almost the same during the experiment for each formation time. Figure 4.3 compares different orifice configurations with the same  $L/D$ . It can be noticed that double-orifice configurations lead to turbulent jets with significant mixing, whereas the single-orifice leads to a single vortex ring.

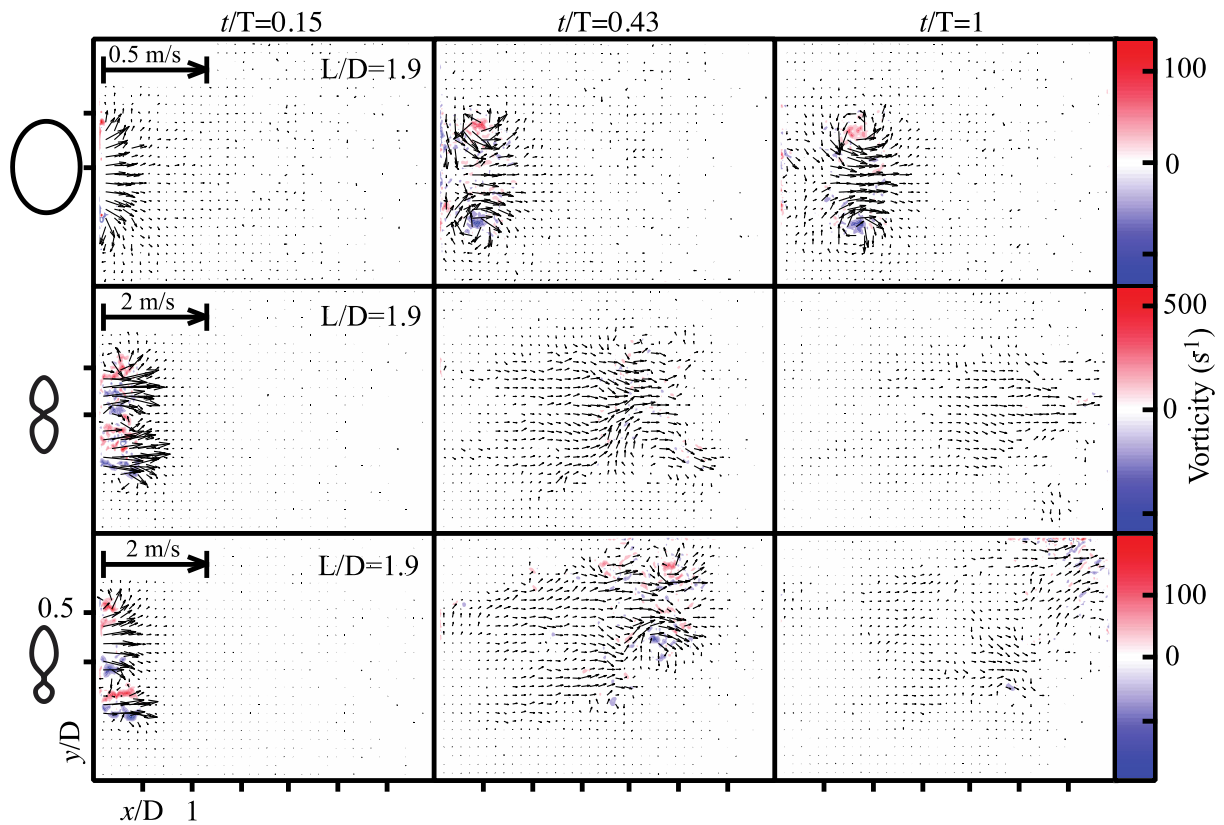


**Figure 4.3** Three MV configurations with  $L/D=1.9$  at different instances are presented. From up to bottom, there are single-orifice MV, symmetric DO MV and asymmetric DO MV

It can also be noticed that the jets in DO configurations travel much faster than the single-orifice configuration. In addition, the magnitude of the velocity and vorticity in DO configurations are much greater than the single-orifice, especially the symmetric DO. Apart from the single-orifice MV, the other double-orifice configurations indicate a vivid decrease in the kinetic energy of the flow during one second of the experiment.

Figure 4.4 displays normalized time-averaged velocity ( $u_{mean}/U$ ) profiles of SO MV, symmetric MV and asymmetric MV at three different locations corresponding to  $x/D$ . Here  $u_{mean}$  is the mean velocity magnitude in time, ( $\sqrt{u^2 + v^2}$  m/s), and  $U$  (m/s) is the mean jet exit velocity.

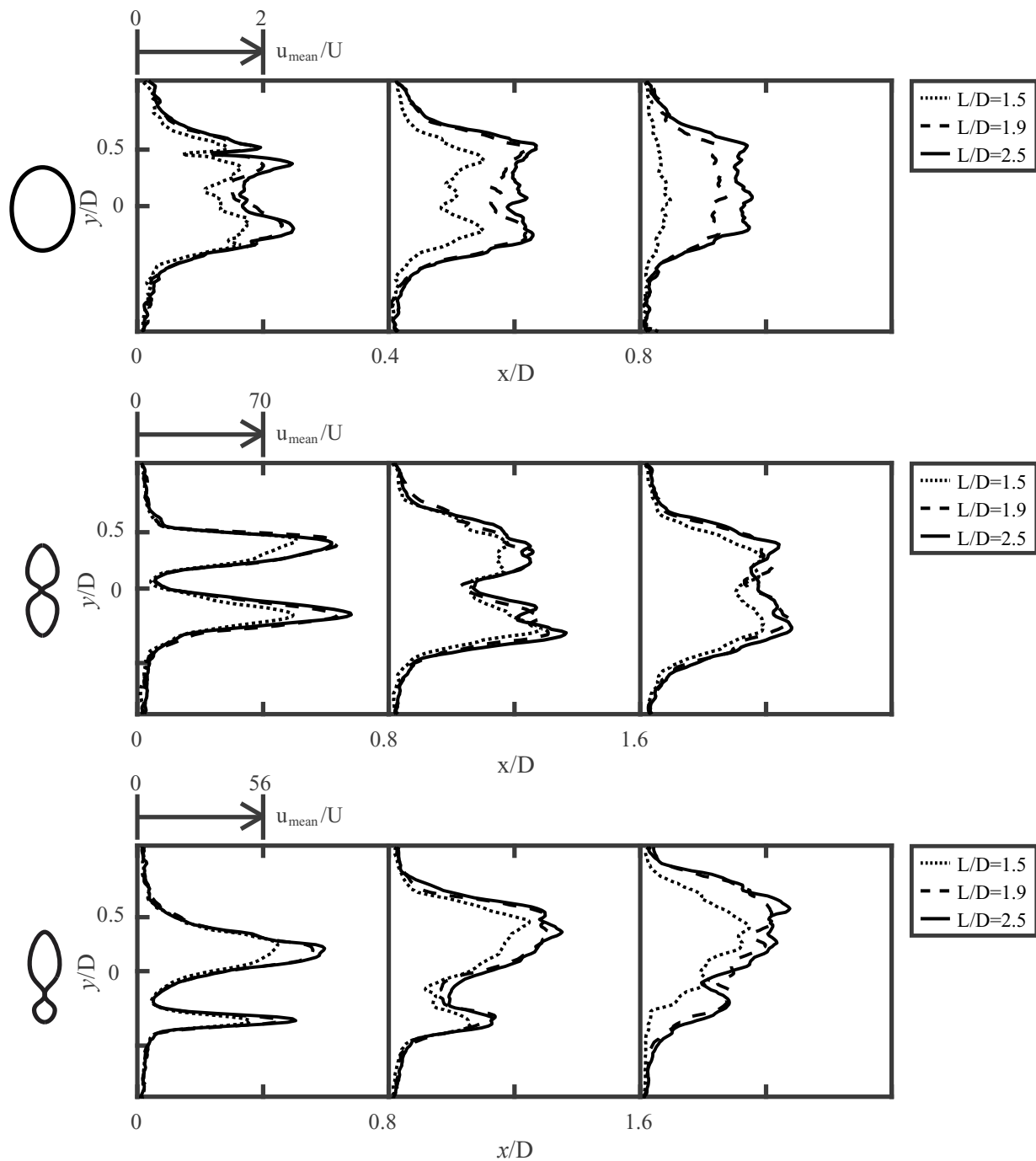


**Figure 4.4** Time-averaged velocity profiles of SO MV, symmetric MV and asymmetric MV

Each case is normalized with respect to mean jet exit velocity of the single-orifice configuration. The single-orifice configuration leads to a flat-like velocity profile, consistent with what is expected downstream of a native healthy mitral valve. However, the DO configuration resulting

from ETER leads to a double jet velocity profile configuration with elevated localized velocity gradients. It is also important to consider to the magnitude of  $u_{mean}$ , which is much larger in DO configurations, especially in symmetric double-orifice configuration. The asymmetric profile tends to shift upward due to weaker pressure in the centerline of the upper jet. Therefore, the smaller jet tends to change the direction of the flow upward.

### 4.3. Analysis of Energy Loss

Viscous energy dissipation is a measure of energy loss in the flow field. Following the work done by Pedrizzetti & Domenichini (2015), Stugaard et al (2018) and Di Labbio (2019), VED for a 2D velocity field is calculated according to the Eq. of 3.13.

From a clinical point-of-view, VED is an important index that reflects spatial dispersion of blood flow and indicates energy dissipation caused by viscosity. In the human heart, an increase in VED leads to an increase in required pumping power of LV. The total kinetic energy is also calculated using the following equation.

$$KE = \frac{\rho}{2} \iint (u^2 + v^2) dx dy \quad (4.1)$$

where  $u$  and  $v$  are velocity components in 2D,  $\rho$  is fluid density. KE and VED are calculated for all the velocity fields. For better illustration, the first IMF of EMD which contains the high frequencies are removed from VED/KE signals. Figure 4.5, on the left side, displays the time evolution of KE for all the three MV configurations investigated in this study. The outcome shows that the single-orifice configuration results in a flow with lower kinetic energy in comparison with DO configurations.

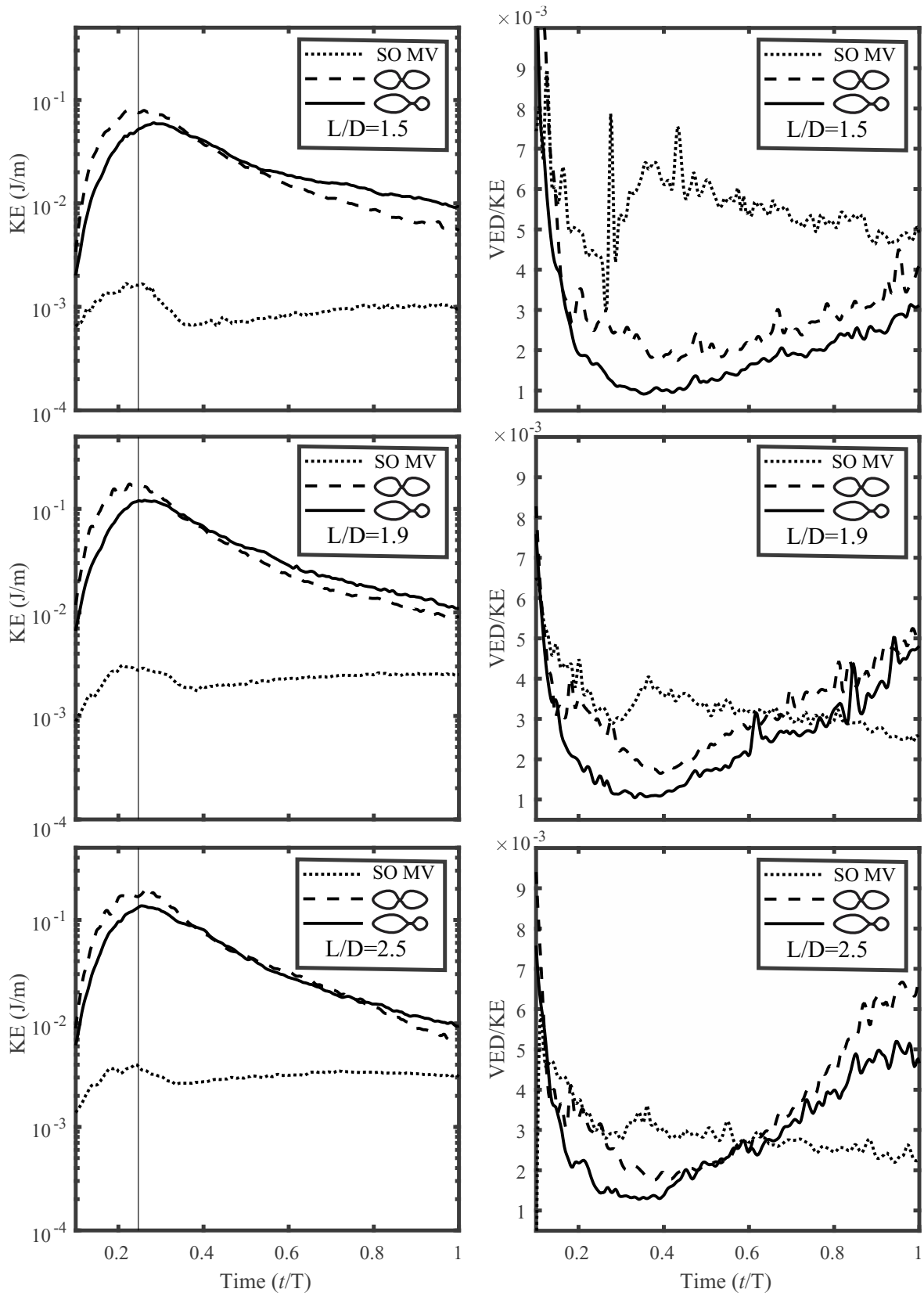


**Figure 4.5** Time evolution of VED/KE on the left and time evolution of KE on the right is plotted.

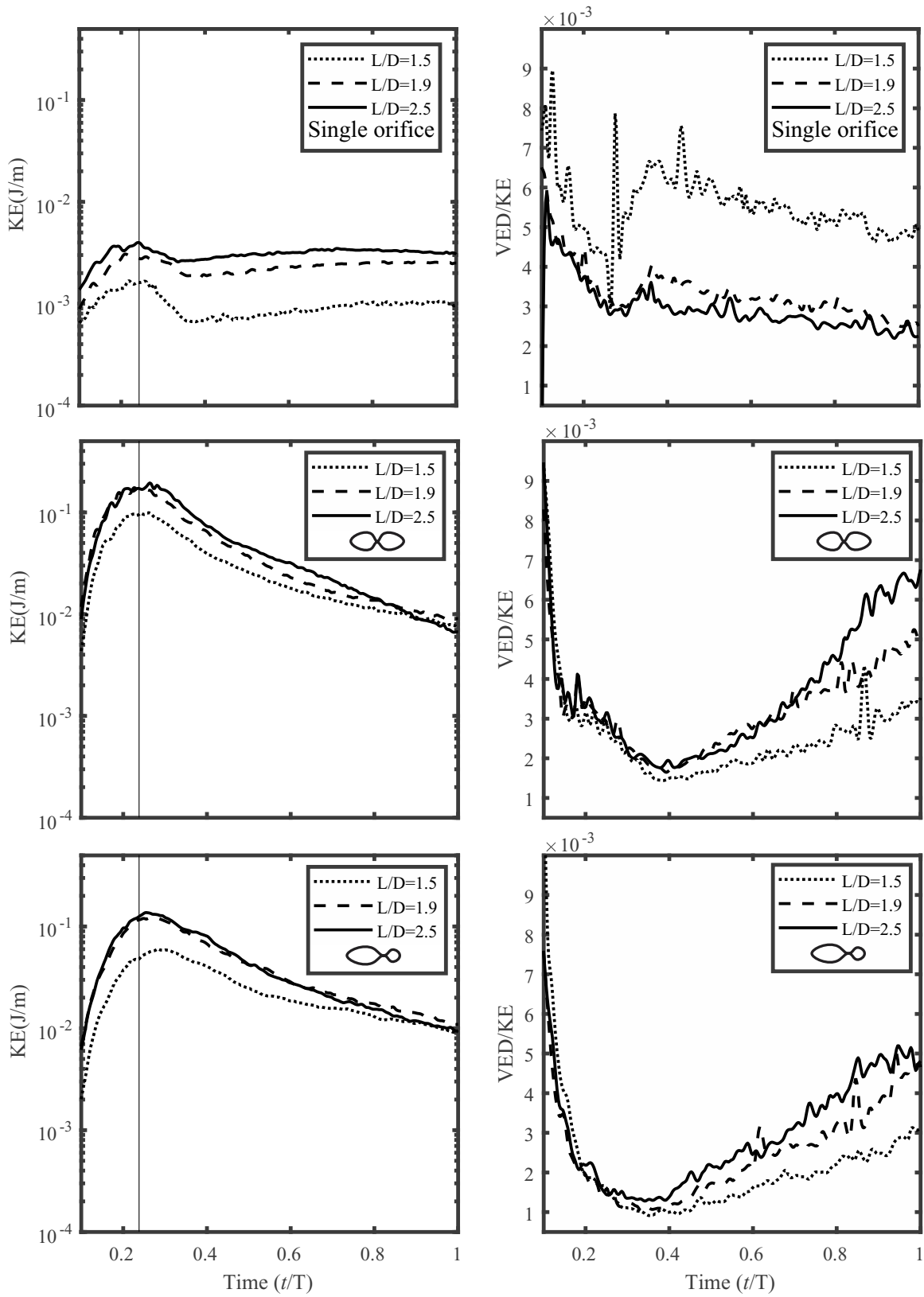


**Figure 4.6** Time evolution of VED/KE on the left and time evolution of KE on the right is plotted

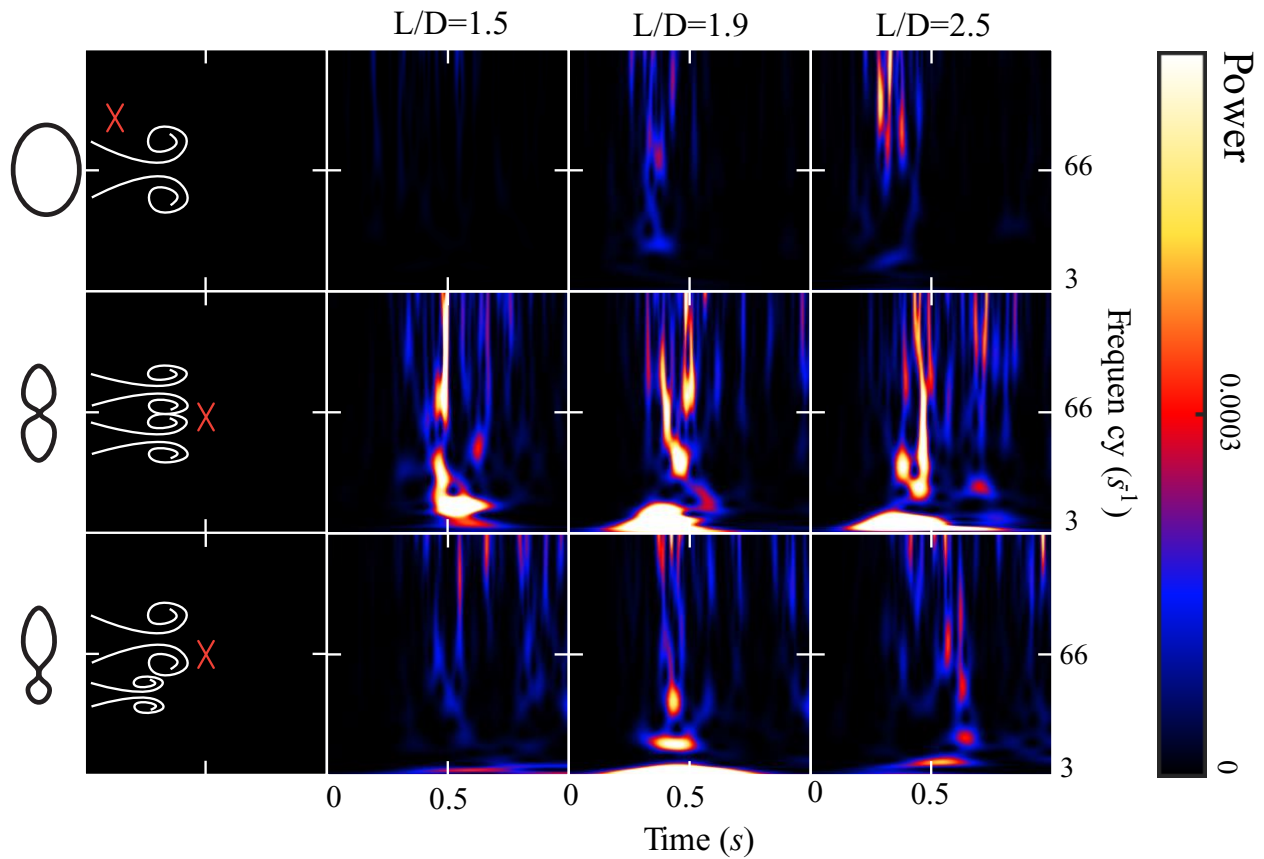
Also, after the piston stops at  $t/T = 0.25$ , the vertical line in the figure, this energy is conserved quite well because it is transported by the vortex ring. This is not the case for the double-orifice configurations where high kinetic energy values are generated during piston movement followed by a smooth decay. Figure 4.5, on right side, shows that this decay is due to a more significant contribution of viscous energy dissipation resulting from the turbulent mixing downstream of the orifice. It is also interesting that the highest KE belongs to symmetric DO. However, it decreases faster than asymmetric DO configuration.

Figure 4.6 is basically the same as Fig. 4.5 except the sorting. It shows that VED/KE trend is vice versa in single-orifice. In double-orifice configuration, the highest amount of VED/KE is associated with highest formation time, whereas, in the single-orifice configuration the lowest formation time has the most VED/KE.

#### **4.4. Time-Frequency Analysis**

In order to investigate turbulence in the flow, the time-frequency spectra of velocity signals at various points are analyzed using continuous wavelet transform. For this purpose, complex Morlet wavelet is used for all cases.

In Fig. 4.7, one signal is extracted from each case. For the single-orifice, the point for the signal extraction is chosen near the exit in the shear layer. However, for the double-orifice configurations, the point for the signal is chosen in the middle of the area of interrogation, where two jets are interacting in both DO configurations. Only the time-frequency spectra for the  $u$ -component signal is presented in this research due to its similarity to the  $v$ -component. For the single-orifice, high frequencies which might indicate a mild turbulence, are observed around the time of  $t/T = 0.3$ .



**Figure 4.7** Time frequency spectra of the  $u$ -component. The  $x$  marks show the points where the signal is obtained

Also, it can be observed that the power of the high frequencies with larger formation time is greater. For the simplicity of comparison, one power scale is considered for all nine cases. However, wide bright areas in DO configurations indicate greater magnitude of power. It is also important to consider the position of the points for signals. The points in DO configuration cases are in the middle of AOI. Therefore, the power of frequencies is decreased significantly. This point can be seen clearly in Fig. 4.8. However, the power of high frequencies in DO configurations is still much greater than the single-orifice. In the symmetric DO, the flow in the center is characterized by dominant low frequency variations with sustained turbulence for a long period.

Whereas in SO, the dominant characteristic of the flow is described by higher frequencies in a short period.

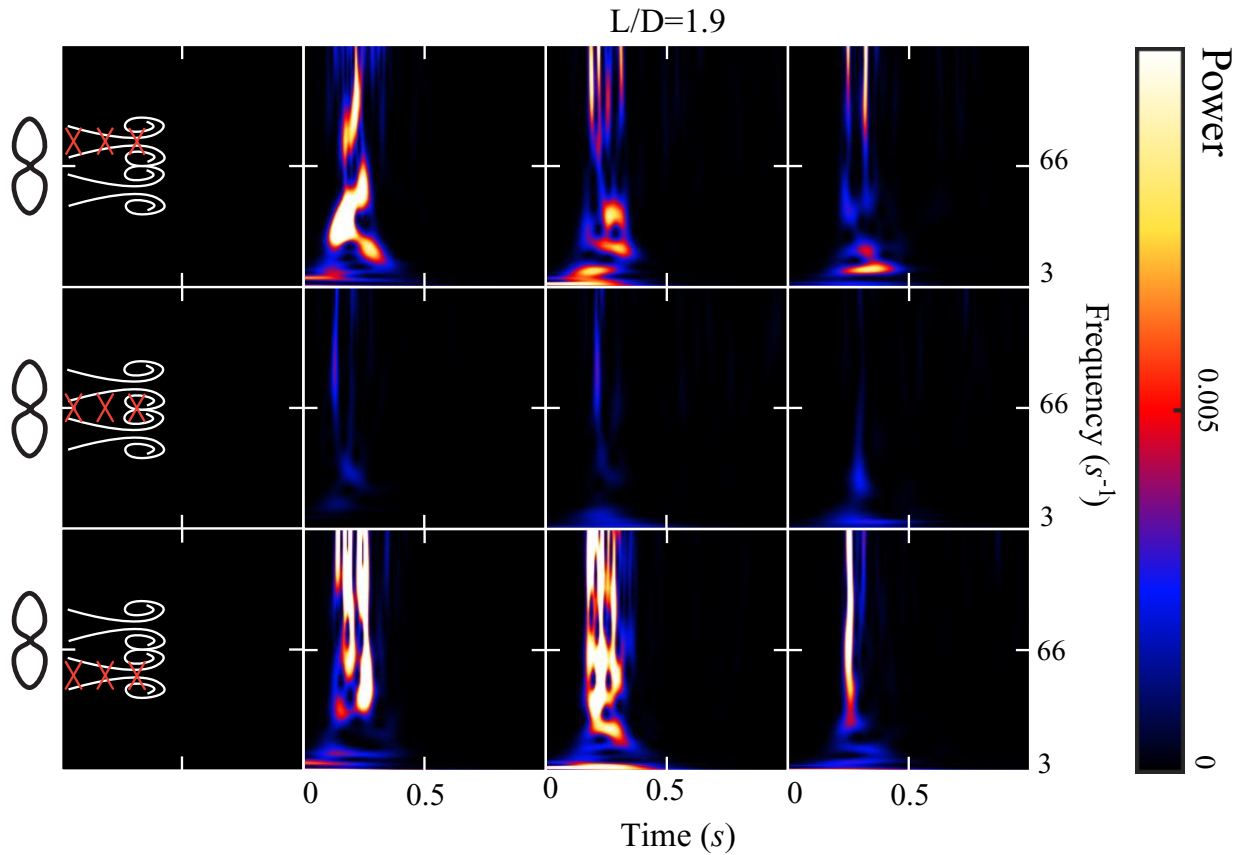


**Figure 4.8** Time frequency spectra of the  $u$ -component for symmetric DO with  $L/D=1.9$  for nine points

It is worth mentioning that by considering more points for each case, the highest powers in high frequency regions are observed in symmetric double-orifice configuration.

Figure 4.8 shows how the amplitude of signals changes in the direction of the flow. It also displays the points in the flow where two jets start to interact in symmetric double-orifice. Due to similarity of cases with different  $L/D$ , only  $L/D=1.9$  is displayed for discussion. The velocity signals within the jet cores in the symmetric double-orifice configuration are rather turbulent, being strongly

comprised of high frequencies. The region between the cores, although exhibiting significant shear, does not experience strong turbulence but is instead dominated by lower frequencies.

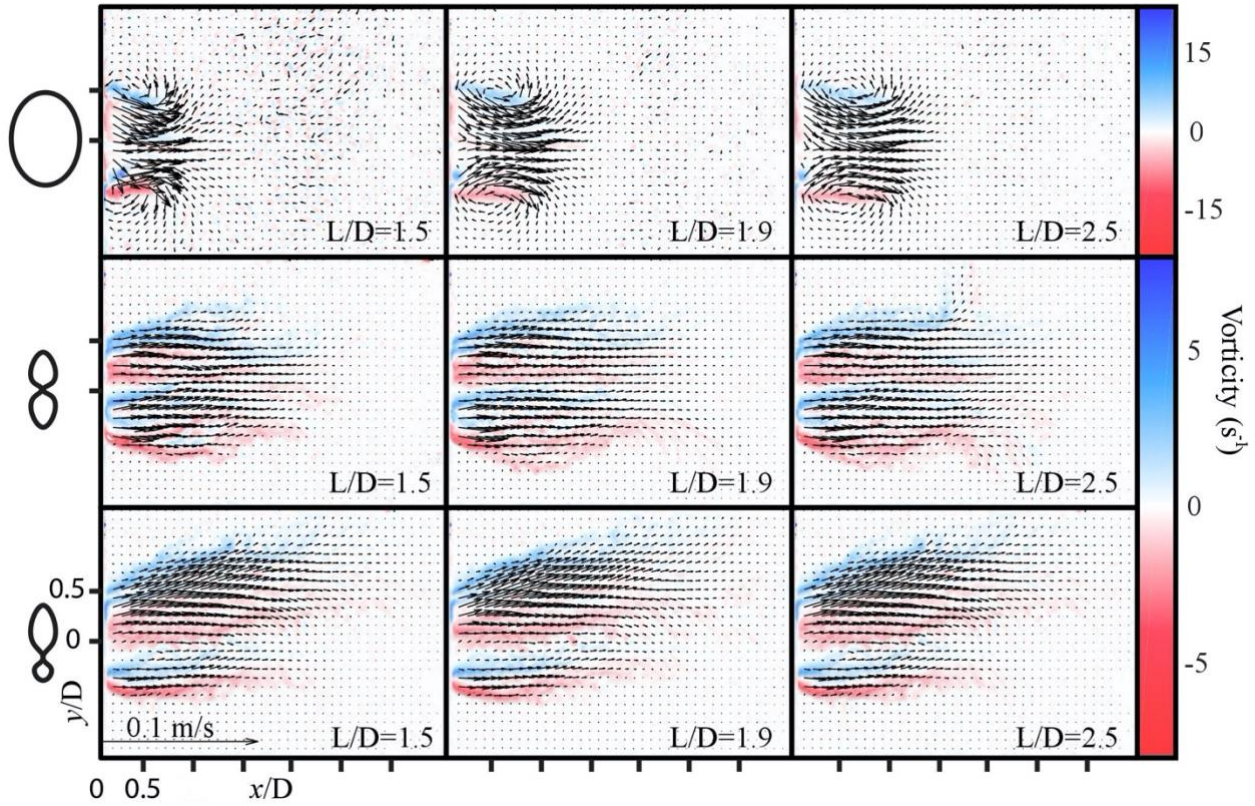
One can observe that the power of high frequencies in the flow direction is decreased dramatically, which agrees with findings in Fig. 4.3. In Fig. 4.3 the magnitude of velocity in DO configurations are decreased in x direction. Therefore, signals obtained from downstream have less amplitude.

## 4.5. Proper Orthogonal Decomposition

To reconstruct a model according to the leading number of modes required to capture 95% and 99% of the flow kinetic energy, the modes are ranked according to their kinetic energy content. For the purposes of flow reconstruction, we can simply multiply the columns of the matrix  $\Phi$  in Eq. 3.18 (i.e., spatial modes) to the correspondent rows of matrix  $\mathbf{B}$  Eq. 3.19 (i.e., temporal modes) to capture the desired energy.

In this study, the first proper orthogonal modes, i.e., average modes, for the single-orifice capture 34.7%, 42.9% and 43% of the energy for the formation time of 1.5, 1.9 and 2.5, respectively. For the symmetric double-orifice configuration, the first proper orthogonal modes capture 51.7%, 50.7% and 51.1% for the same formation times. First POD modes for the asymmetric configuration capture 44.2%, 48.1% and 49.8% of the total energy for the same formation numbers.

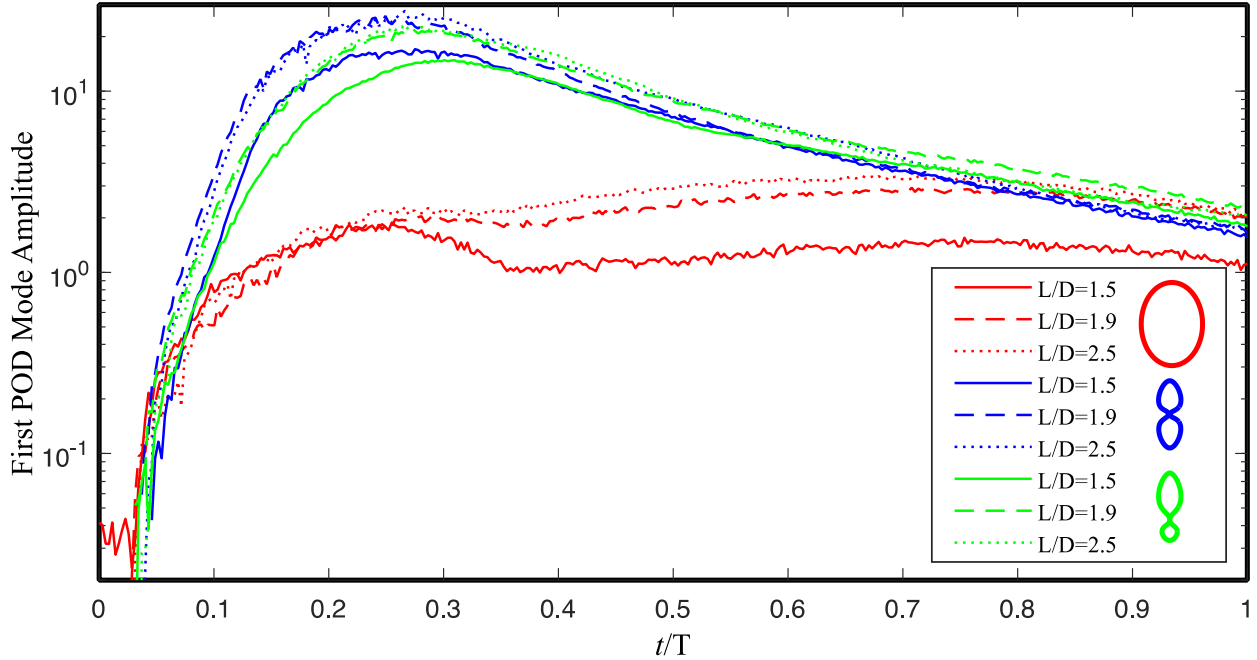
The first four modes along with their amplitudes for each configuration, i.e., SO, SDO, ADO, are presented for  $L/D=1.9$  in the appendix. The time-averaged velocity fields, which are representative of the first POD spatial modes, are shown in Fig. 4.9 for all cases.



**Figure 4.9** Time-averaged velocity field and vorticity for all the configurations

As it can be seen from the Fig. 4.9, the first POD mode represents a single vortex ring evolving in time for the single-orifice configuration. However, first POD mode in other configurations has not captured the structure of the flow due to the relatively high velocity magnitudes of the flow. Also, it seems that the flow in asymmetric configurations are shifted upward due to the lower pressure of the primary jet and merging of the smaller jet.

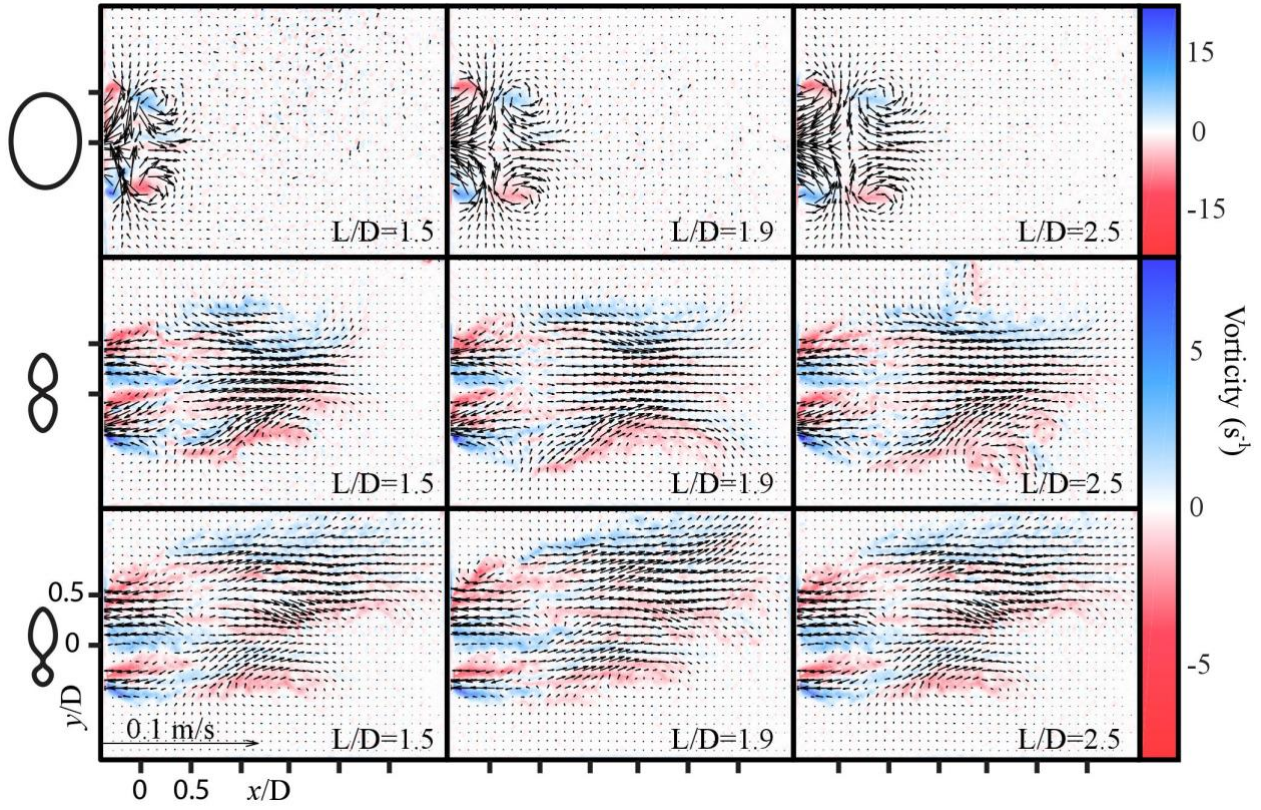
Since the spatial modes are orthonormal, the magnitude of the velocities in the first POD modes of all cases are comparable in the same scale. However, as the Fig. 4.10 shows, the magnitude of the first temporal modes in double-orifice configurations is much higher than the single-orifice.



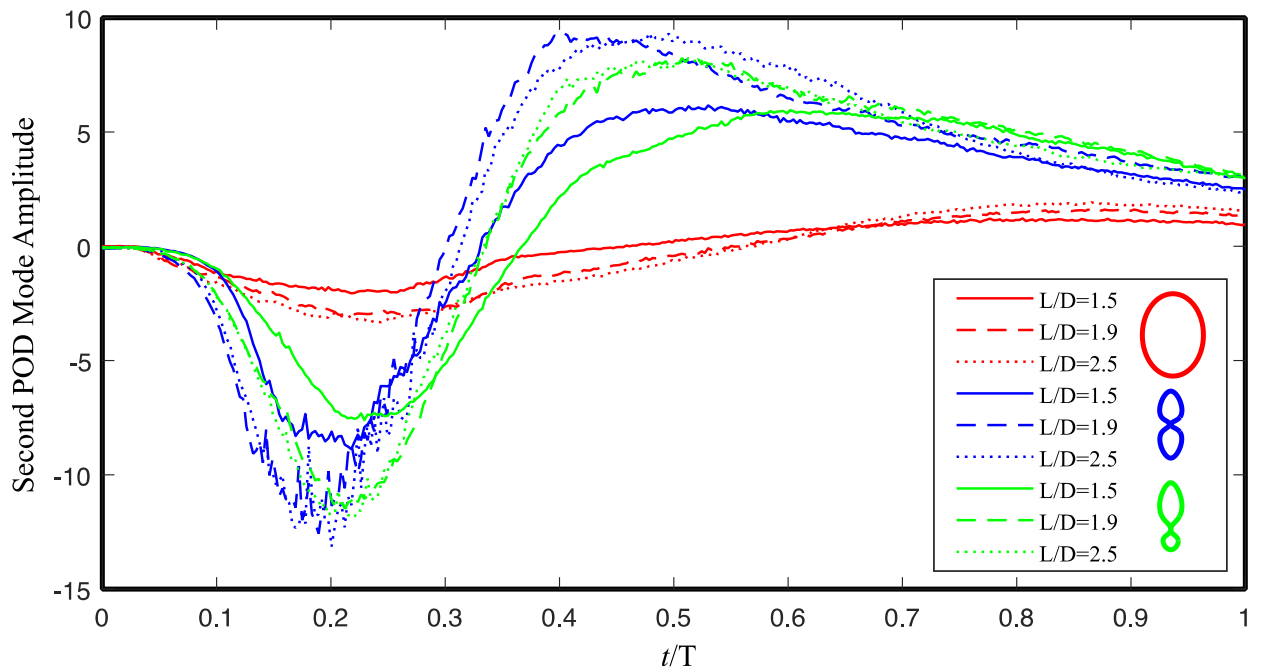
**Figure 4.10** Temporal dynamics of the first POD modes

Figure 4.10 shows by increasing the formation time in the single configuration, the amplitude of the first POD mode is increased. Whereas, the trend is vice versa in double-orifice configurations. The results agree with the findings from Fig. 4.6, where the dissipation of the energy is decreased by increasing the formation time in single-orifice configuration. This means that the amplitude of the velocities in the vortex ring of the single configuration is more constant when the formation time is higher. Also, the local maxima of the amplitude are around the time where the piston stops,  $t/T = 0.25$ , and  $t/T = 0.75$ .

The results of the second spatial and temporal modes are displayed in Figs. 4.11 and 4.12, demonstrate features associated with the progression of the flow. The amplitude of the second temporal modes is again higher in double configurations.



**Figure 4.11** Second spatial POD mode and vorticity for all the configurations



**Figure 4.12** Temporal dynamics of the second POD modes

Fraction of total kinetic energy shown in Fig. 4.13 reveals a slow convergence to the total energy in all cases due to the streamwise velocity. Interestingly, for the single-orifice, the trend is vice versa when the formation time is increased, i.e., the fraction of total kinetic energy is increased by increasing the formation time in the single-orifice. Therefore, even though the vortex ring travels faster when the formation time is higher, i.e.  $L/D=2.5$ , POD captures more energy in the first POD mode and convergence is faster. This might be due to the higher VED in lower formation times which is reflected as higher amplitude of the first POD mode. To compare the double configurations, figure 4.13 shows that the first POD mode has the highest energy in symmetric configuration with  $L/D=1.5$ . It also seems that the first POD mode in symmetric configuration has higher amplitude in comparison with other configurations.

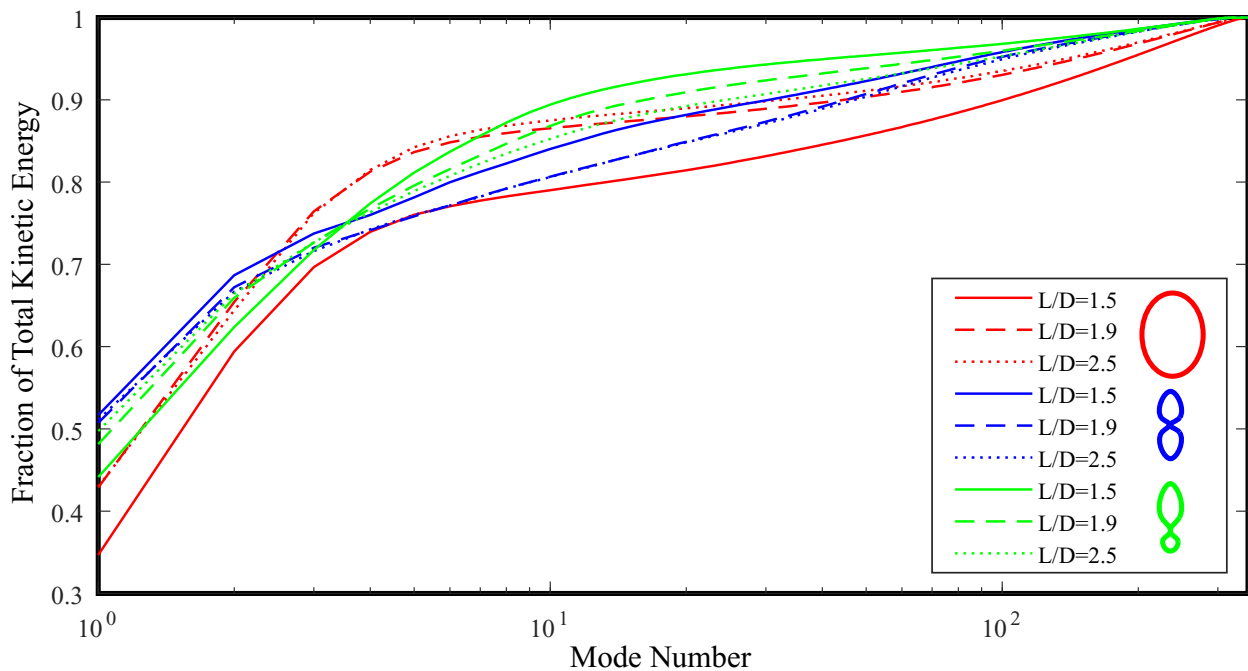


**Figure 4.13** The fraction of accumulated kinetic energy against mode number

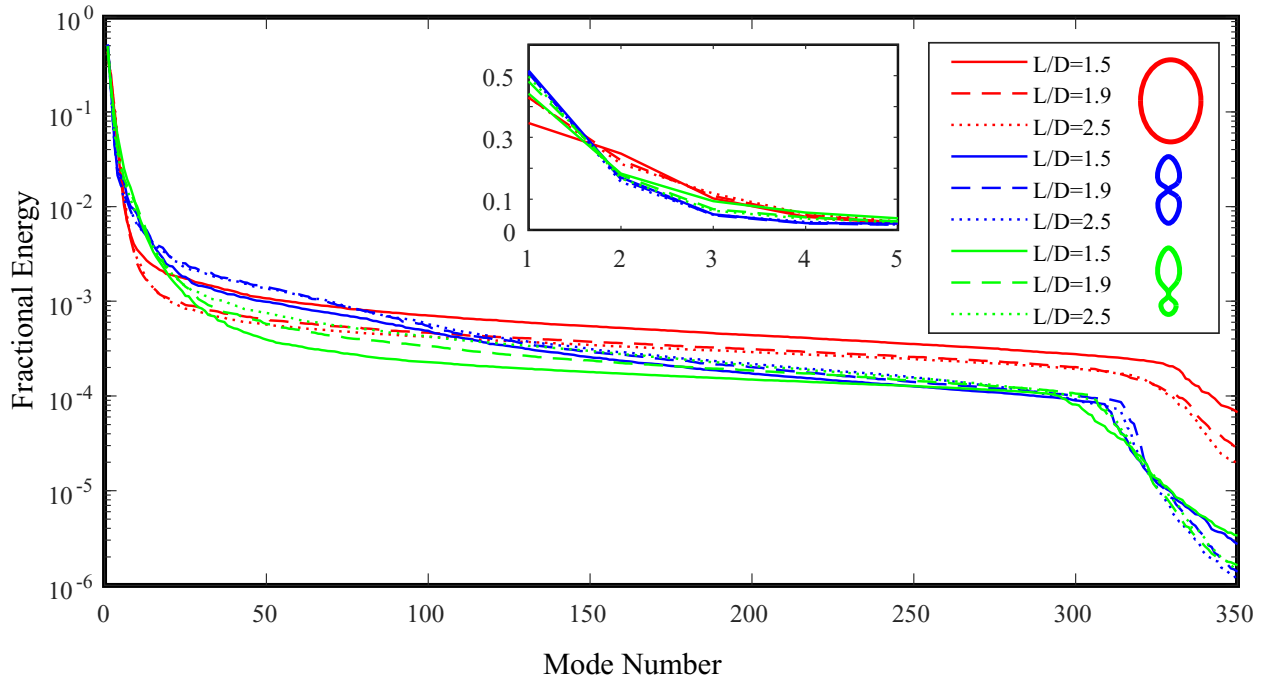


**Figure 4.14** The fractional kinetic energy against mode number. First five modes are plotted separately

However, the convergence is slower in the symmetric configuration in comparison with asymmetric one, which indicates more changes and complexity in the structure of the flow and/or higher velocity of the flow in that case.

Figure 4.14 also shows the energy associated with each mode. It is observed that for a large number of modes, i.e., 50 to 300, the energy does not vary so much, which is due to the moving structure of the flow. Also, a drop of energy at the end can be identified due to the noises and incoherent structures. Because of the nature of the flow with transitional streamwise velocity, we need relatively a large number of the modes to reconstruct the flow up to 95% and 98% of the kinetic energy. Also, It can be seen that only the first three modes in each configuration has more than 10% of energy.

**Table 4.2** Number of modes required to capture the desired kinetic energy

<i>Formation time</i>	Single-orifice configuration		Symmetric configuration		Asymmetric configuration	
	95%	98%	95%	98%	95%	98%
1.5	198	266	85	170	41	160
1.9	146	240	96	182	74	179
2.5	138	237	101	187	93	186

Table 4.2 demonstrates a summary of the modes required to reconstruct the flow up to desired kinetic energy. It seems that the asymmetric configuration requires the least number of the modes to reconstruct the flow according to the level of kinetic energy. Which means the single-orifice configuration with its almost constant structure through the experiment, i.e., 1s, needs more modes to be reproduced up to a relatively high amount of kinetic energy. A close look at Fig. 4.14 clears why we need more modes to reconstruct the single orifice configuration flow. It can be seen that we need less modes to reconstruct the flow in single orifice and most of the modes which have about the same kinetic energy are explaining the movement of the flow to downstream. By knowing this fact, it is true to say the structure of the flow in single orifice configuration requires the least number of modes to be explained. In contrast, we need the most number of the modes to explain the structure of the flow in symmetric configuration.

## 5. Conclusions and Recommendations

The flow downstream of the left ventricle after ETER is rarely studied in the literature. In this work, the flow structures in the near-field wake of a model of a mitral valve are investigated before and after simulating ETER. Time-averaged velocity profiles show that the two jets merge at the downstream in double-orifice configurations. Also, the investigation on the path of the vortices in the single-orifice configurations shows a steady streamwise velocity of cores throughout the experiments. After examining viscous energy dissipation and time-frequency spectra for several points in the flow, it is observed that asymmetric double-orifice leads to less dissipation and turbulence compared to symmetric one. The results agree with the research done by Chetina (2015). She investigated the dynamics of a jet emerging from different orifice configurations. In that experiment, the flow emerging from twin jets had the most energy consumption. This finding is interesting because symmetric configuration is the case used the most in ETER surgeries. Therefore, the information obtained through this study is useful to improve existing MV repair technique. POD analysis reveal that the asymmetric configuration requires the least number of modes to be reconstructed up to desired level of energy. Time-frequency analysis of the signals extracted from symmetric configuration indicates strong turbulence in the centerline of the jets, whereas the turbulence is not strong are the two jets interacted.

For future work, it is important to address the effects of the jets' boundary conditions. Therefore, substituting the large water tank with a chamber to closely resemble the left ventricle would be essential. Furthermore, use of a 3D PIV would be highly beneficial for investigating the turbulence in the flow of a model mitral valve.

## References

- Addison, P. S. (2017). *The Illustrated Wavelet Transform Handbook: Introductory Theory and Applications in Science, Engineering, Medicine and Finance*. CRC Press.
- Allen, J. J., & Auvity, B. (2002). Interaction of a vortex ring with a piston vortex. *Journal of Fluid Mechanics*, 465, 353-378.
- Alfieri, O., Maisano, F., De Bonis, M., Stefano, P. L., Torracca, L., Oppizzi, M., & La Canna, G. (2001). The double-orifice technique in mitral valve repair: a simple solution for complex problems. *Journal of Thoracic and Cardiovascular Surgery*, 122(4), 674-681.
- Anderson, E. A., & Spall, R. E. (2001). Experimental and numerical investigation of two-dimensional parallel jets. *Journal of Fluids Engineering*, 123(2), 401-406.
- Barbieri, A., Bursi, F., Grigioni, F., Tribouilloy, C., Avierinos, J.F., Michelena, H.I., Rusinaru, D., Szymansky, C., Russo, A., Suri, R. & Bacchi Reggiani, M.L. (2011). Prognostic and therapeutic implications of pulmonary hypertension complicating degenerative mitral regurgitation due to flail leaflet: a multicenter long-term international study. *European Heart Journal*, 32(6), 751-759.
- Berkooz, G., Holmes, P., & Lumley, J. L. (1993). The proper orthogonal decomposition in the analysis of turbulent flows. *Annual Review of Fluid Mechanics*, 25(1), 539-575.
- Białeckı, R. A., Kassab, A. J., & Fic, A. (2005). Proper orthogonal decomposition and modal analysis for acceleration of transient FEM thermal analysis. *International Journal for Numerical Methods in Engineering*, 62(6), 774-797.
- Bonow, R. O., Carabello, B., De Leon, A. C., Edmunds, L. H., Fedderly, B. J., Freed, M. D., ... & O'Rourke, R. A. (1998). ACC/AHA guidelines for the management of patients with valvular heart disease. Executive summary. A report of the American College of Cardiology/American Heart Association Task Force on Practice Guidelines (Committee on Management of Patients With Valvular Heart Disease). *The Journal of Heart Valve Disease*, 7(6), 672-707.
- Choi, S. M., Kim, W. H., Côté, D., Park, C. W., & Lee, H. (2011). Blood cell assisted in vivo Particle Image Velocimetry using the confocal laser scanning microscope. *Optics Express*, 19(5), 4357-4368.
- Di Labbio, G., & Kadem, L. (2019). Reduced-order modeling of left ventricular flow subject to aortic valve regurgitation. *Physics of Fluids*, 31(3), 031901.
- Di Fonso, A., Bartoloni, G., Calafiore, A.M., Di Baldassarre, A. & Italian Group of Study for Heart Valve Disease (Italian Society of Cardiology. (2013). Functional mitral regurgitation: from normal to pathological anatomy of mitral valve. *International Journal of Cardiology*, 163(3), 242-248.
- Ducas, R. A., White, C. W., Wassef, A. W., Farag, A., Bhagirath, K. M., Freed, D. H., & Tam, J. W. (2014). Functional mitral regurgitation: current understanding and approach to management. *Canadian Journal of Cardiology*, 30(2), 173-180.

- Durve, A., Patwardhan, A. W., Banarjee, I., Padmakumar, G., & Vaidyanathan, G. (2012). Numerical investigation of mixing in parallel jets. *Nuclear Engineering and Design*, 242, 78-90.
- Espiritu, D., Onohara, D., Kalra, K., Sarin, E. L., & Padala, M. (2017). Transcatheter mitral valve repair therapies: evolution, status and challenges. *Annals of Biomedical Engineering*, 45(2), 332-359.
- Faludi, R., Szulik, M., D'hooge, J., Herijgers, P., Rademakers, F., Pedrizzetti, G., & Voigt, J. U. (2010). Left ventricular flow patterns in healthy subjects and patients with prosthetic mitral valves: an in vivo study using echocardiographic particle image velocimetry. *Journal of Thoracic and Cardiovascular Surgery*, 139(6), 1501-1510.
- Gharib, M., Rambod, E., & Shariff, K. (1998). A universal time scale for vortex ring formation. *Journal of Fluid Mechanics*, 360, 121-140.
- Gharib, M., Rambod, E., Kheradvar, A., Sahn, D. J., & Dabiri, J. O. (2006). Optimal vortex formation as an index of cardiac health. *Proceedings of the National Academy of Sciences*, 103(16), 6305-6308.
- Gillinov, A. M., Blackstone, E. H., Nowicki, E. R., Slisatkorn, W., Al-Dossari, G., Johnston, D. R., ... & Svensson, L. G. (2008). Valve repair versus valve replacement for degenerative mitral valve disease. *The Journal of Thoracic and Cardiovascular Surgery*, 135(4), 885-893.
- Ghosh, E., & Kovács, S. J. (2011). E-wave associated vortex formation facilitates diastatic mitral leaflet coaptation. *Journal of the American College of Cardiology*, 57(14 Supplement), E663.
- Goel, S. S., Bajaj, N., Aggarwal, B., Gupta, S., Poddar, K. L., Ige, M., Bdair, H., Anabtawi, A., Rahim, S., Whitlow, P.L. & Tuzcu, E. M. (2014). Prevalence and outcomes of unoperated patients with severe symptomatic mitral regurgitation and heart failure: comprehensive analysis to determine the potential role of MitraClip for this unmet need. *Journal of the American College of Cardiology*, 63(2), 185-186.
- Grigioni, F., Avierinos, J. F., Ling, L. H., Scott, C. G., Bailey, K. R., Tajik, A. J., ... & Enriquez-Sarano, M. (2002). Atrial fibrillation complicating the course of degenerative mitral regurgitation: determinants and long-term outcome. *Journal of the American College of Cardiology*, 40(1), 84-92.
- Hall, J. E. (2015). *Guyton & Hall Physiology Review E-Book*. Elsevier Health Sciences.
- Holubec, T., Sündermann, S. H., Jacobs, S., & Falk, V. (2013). Chordae replacement versus leaflet resection in minimally invasive mitral valve repair. *Annals of Cardiothoracic Surgery*, 2(6), 809.
- Hotelling, H. (1933). Analysis of a complex of statistical variables into principal components. *Journal of Educational Psychology*, 24(6), 417.
- Hu, Y., Shi, L., Parameswaran, S., Smirnov, S., & He, Z. (2010). Left ventricular vortex under mitral valve edge-to-edge repair. *Cardiovascular Engineering and Technology*, 1(4), 235-243.
- Huang, N. E., Shen, Z., Long, S. R., Wu, M. C., Shih, H. H., Zheng, Q., Yen, N.C., Tung, C.C. & Liu, H. H. (1998). The empirical mode decomposition and the Hilbert spectrum for nonlinear and

non-stationary time series analysis. *Proceedings of the Royal Society of London. Series A: Mathematical, Physical and Engineering Sciences*, 454(1971), 903-995.

Jolley, M. A., Ghelani, S. J., Adar, A., & Harrild, D. M. (2017). Three-dimensional mitral valve morphology and age-related trends in children and young adults with structurally normal hearts using transthoracic echocardiography. *Journal of the American Society of Echocardiography*, 30(6), 561-571.

Kaul, S. (2004). The extents of mitral leaflet opening and closure are determined by left ventricular systolic function.

Kerschen, G., Poncelet, F., & Golinval, J. C. (2007). Physical interpretation of independent component analysis in structural dynamics. *Mechanical Systems and Signal Processing*, 21(4), 1561-1575.

Koller-Milojevic, D., & Schneider, W. (1993). Free and confined jets at low Reynolds numbers. *Fluid Dynamics Research*, 12(6), 307.

Kundu, P. K., Cohen, I. M., & Dowling, D. R. (2012). Chapter 12-Turbulence. *Fluid Mechanics (Fifth Edition)*, Academic Press, Boston, 541-620.

Kutz, J. N., Brunton, S. L., Brunton, B. W., & Proctor, J. L. (2016). *Dynamic mode decomposition: data-driven modeling of complex systems*. Society for Industrial and Applied Mathematics.

Liang, Y. C., Lee, H. P., Lim, S. P., Lin, W. Z., Lee, K. H., & Wu, C. G. (2002). Proper orthogonal decomposition and its applications—Part I: Theory. *Journal of Sound and vibration*, 252(3), 527-544.

Ly, H. V., & Tran, H. T. (2001). Modeling and control of physical processes using proper orthogonal decomposition. *Mathematical and Computer Modelling* 33, 223–236.

Maisano, F., Redaelli, A., Pennati, G., Fumero, R., Torracca, L., & Alfieri, O. (1999). The hemodynamic effects of double-orifice valve repair for mitral regurgitation: a 3D computational model. *European Journal of Cardio-Thoracic Surgery*, 15(4), 419-425.

Maisano, F., Schreuder, J. J., Oppizzi, M., Fiorani, B., Fino, C., & Alfieri, O. (2000). The double-orifice technique as a standardized approach to treat mitral regurgitation due to severe myxomatous disease: surgical technique. *European Journal of Cardio-Thoracic Surgery*, 17(3), 201-205.

McCarthy, K. P., Ring, L., & Rana, B. S. (2010). Anatomy of the mitral valve: understanding the mitral valve complex in mitral regurgitation. *European Journal of Echocardiography*, 11(10), i3-i9.

Melling, A. (1997). Tracer particles and seeding for particle image velocimetry. *Measurement Science and Technology*, 8(12), 1406.

Meyer, K. E., Pedersen, J. M., & Özcan, O. (2007). A turbulent jet in crossflow analysed with proper orthogonal decomposition. *Journal of Fluid Mechanics*, 583, 199-227.

- Murashita, T., Greason, K. L., Suri, R. M., Daly, R. C., Joyce, L. D., Stulak, J. M., Pochettino, A., Joyce, D.L., Dearani, J.A. & Schaff, H. V. (2016). Mitral valve gradient after valve repair of degenerative regurgitation with restrictive annuloplasty. *The Journal of Thoracic and Cardiovascular Surgery*, 151(1), 106-109.
- Pedrizzetti, G., & Sengupta, P. P. (2015). Vortex imaging: new information gain from tracking cardiac energy loss. *European Heart Journal*, 16, 719-720.
- Pearson, K. (1901). LIII. On lines and planes of closest fit to systems of points in space. *The London, Edinburgh, and Dublin Philosophical Magazine and Journal of Science*, 2(11), 559-572.
- Perloff, J. K., & Roberts, W. C. (1972). The mitral apparatus: functional anatomy of mitral regurgitation. *Circulation*, 46(2), 227-239.
- Perrin, R., Braza, M., Cid, E., Cazin, S., Barthet, A., Sevrain, A., Mockett, C. & Thiele, F. (2007). Obtaining phase averaged turbulence properties in the near wake of a circular cylinder at high Reynolds number using POD. *Experiments in Fluids*, 43(2-3), 341-355.
- Raffel, M., Willert, C. E., Scarano, F., Kähler, C. J., Wereley, S. T., & Kompenhans, J. (2018). *Particle Image Velocimetry: a Practical Guide*. Springer.
- Richardson, L. F. (2007). *Weather Prediction by Numerical Process*. Cambridge University Press.
- Rogers, J. H., & Franzen, O. (2011). Percutaneous edge-to-edge MitraClip therapy in the management of mitral regurgitation. *European Heart Journal*, 32(19), 2350-2357.
- Rowley, C. W., Mezić, I., Bagheri, S., Schlatter, P., & Henningson, D. S. (2009). Spectral analysis of nonlinear flows. *Journal of Fluid Mechanics*, 641, 115-127.
- Ruotolo, R., & Surace, C. (1999). Using SVD to detect damage in structures with different operational conditions. *Journal of Sound and Vibration*, 226(3), 425-439.
- Schmid, P. J. (2010). Dynamic mode decomposition of numerical and experimental data. *Journal of Fluid Mechanics*, 656, 5-28.
- Sirovich, L. (1987). Turbulence and the dynamics of coherent structures. I. Coherent structures. *Quarterly of Applied Mathematics*, 45(3), 561-571.
- Sirovich, L., & Kirby, M. (1987). Low-dimensional procedure for the characterization of human faces. *Josa a*, 4(3), 519-524.
- Sotiropoulos, F., Le, T. B., & Gilmanov, A. (2016). Fluid mechanics of heart valves and their replacements. *Annual Review of Fluid Mechanics*, 48, 259-283.
- Stugaard, M., Koriyama, H., Katsuki, K., Masuda, K., Asanuma, T., Takeda, Y., Sakata, Y., Itatani, K. & Nakatani, S. (2015). Energy loss in the left ventricle obtained by vector flow mapping as a new quantitative measure of severity of aortic regurgitation: a combined experimental and clinical study. *European Heart Journal-Cardiovascular Imaging*, 16(7), 723-730.

- Tang, D., Kholodar, D., Juang, J. N., & Dowell, E. H. (2001). System identification and proper orthogonal decomposition method applied to unsteady aerodynamics. *AIAA Journal*, 39(8), 1569-1576.
- Tu, J. H., Rowley, C. W., Luchtenburg, D. M., Brunton, S. L., & Kutz, J. N. (2013). On dynamic mode decomposition: Theory and applications. *arXiv preprint arXiv:1312.0041*.
- Tu, J. H., Rowley, C. W., Kutz, J. N., & Shang, J. K. (2014). Spectral analysis of fluid flows using sub-Nyquist-rate PIV data. *Experiments in Fluids*, 55(9), 1805.
- Vahanian, A., Alfieri, O., Andreotti, F., Antunes, M. J., Barón-Esquivias, G., Baumgartner, H., Borger, M.A., Carrel, T.P., De Bonis, M. & Evangelista, A. (2012). Guidelines on the management of valvular heart disease (version 2012) The Joint Task Force on the Management of Valvular Heart Disease of the European Society of Cardiology (ESC) and the European Association for Cardio-Thoracic Surgery (EACTS). *European Heart Journal*, 33(19), 2451-2496.
- Vouros, A., & Panidis, T. (2008). Influence of a secondary, parallel, low Reynolds number, round jet on a turbulent axisymmetric jet. *Experimental Thermal and Fluid Science*, 32(8), 1455-1467.
- Waite, L., & Fine, J. M. (2007). *Applied Biofluid Mechanics*, New York: McGraw Hill Book Co.
- Zang, B., & New, T. H. (2015). On the wake-like vortical arrangement and behaviour associated with twin jets in close proximity. *Experimental Thermal and Fluid Science*, 69, 127-140.

# Appendix

This function converts VEC format to X matrix.

---

```
>> function X=VECToX(VEC)
>> SN=length(VEC); % Number of snapshots
>> [ny,nx] = size(VEC{1}.X); % Size of the velocity matrix
>> u = zeros(nx*ny,SN); % Initial matrix of streamwise velocity
>> v = zeros(nx*ny,SN); % Initial matrix of transverse velocity
>> for i=1:SN % creating u and v matrices
>>     u(:,i)=VEC{i}.U(:);
>>     v(:,i)=VEC{i}.V(:);
>> end
>> X=[u;v]; % creating X matrix
>> end
```

---

This function converts X matrix to VEC format.

---

```
function VECF=XtoVEC(X,VEC)
Sn=length(VEC);
VECF=cell(Sn,1);
for i=1:Sn
    VECF{i}.C=VEC{i}.C;
    VECF{i}.X=VEC{i}.X;
    VECF{i}.Y=VEC{i}.Y;
end
[ny,nx] = size(VEC{1}.X);
m=nx*ny;
for i=1:Sn
    VECF{i}.U=zeros(ny,nx);
    VECF{i}.V=zeros(ny,nx);
    VECF{i}.U(:)=X(1:m,i);
    VECF{i}.V(:)=X(m+1:end,i);
end
end
```

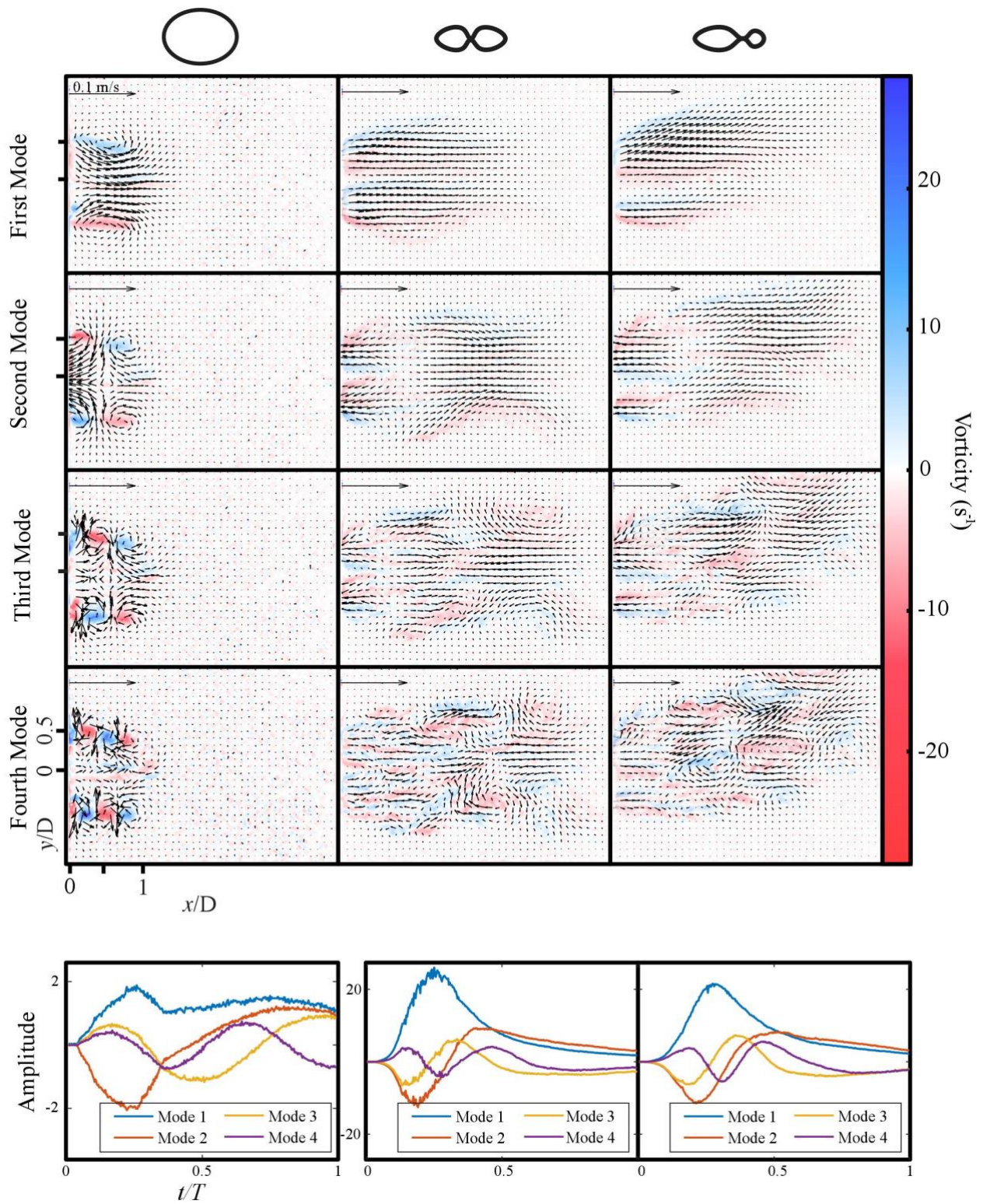
---

This function calculates POD spatial modes, temporal modes and eigenvalues.

---

```
>> function [M, A, S] = POD(X)
>> C=X'*X;
>> [V,S] = eig(C, 'vector');
>> [S,I] = sort(S, 'descend');
>> V = V(:, I. ');
>> M = X*V*diag(S.^(-1/2));
>> A = M'*X;
>> end
```

---



This figure illustrates four POD modes with  $L/D=1.9$  and with three different configurations. The amplitudes of the modes are demonstrated in the bottom panel.